Building and Environment 286 (2025) 113564

Contents lists available at ScienceDirect

Building and Environment

journal homepage: www.elsevier.com/locate/buildenv

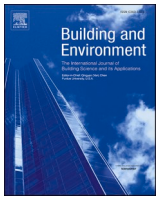

A novel methodology for rapid aging of HVAC filters using a synthetic submicron aerosol: Effects of HVAC system operational and environmental conditions on filter loading

Chunxu Huang [a,b], Nusrat Jung [a,b], Brandon E. Boor [a,b,*]

[a] Lyles School of Civil and Construction Engineering, Purdue University, West Lafayette, IN 47907, United States
[b] Ray W. Herrick Laboratories, Center for High Performance Buildings, Purdue University, West Lafayette, IN 47907, United States

ARTICLE INFO

Keywords:
Standardized HVAC filter test protocols
Air cleaning equipment
Filter loading dynamics
Filtration efficiency
Fine and ultrafine particulate matter
Building ventilation systems
Indoor air quality

ABSTRACT

Heating, ventilation, and air conditioning (HVAC) filters play a critical role in mitigating indoor air pollution while contributing to HVAC system energy consumption by increasing system airflow resistance as they accumulate particles. Their performance is strongly influenced by aerosol physicochemical properties, particularly the particle size distribution (PSD), which affects filter loading behavior and efficiency. However, standardized test protocols primarily use coarse-mode loading dusts that poorly represent the submicron PSDs characteristic of urban aerosol. This study introduces a novel methodology for aging HVAC filters using synthetic submicron potassium chloride (KCl) aerosol generated by burning salt sticks with a thermal aerosol generator integrated with a full-scale HVAC filter test rig. The loading performance of three minimum efficiency reporting value (MERV)-rated filters – MERV8, MERV13, and MERV14 – was evaluated under varying volumetric airflow rates, salt stick feed rates, and relative humidities (RH). Results show that higher airflow rates accelerate clogging, while lower rates extend loading periods and increase salt stick consumption. The salt stick feed rate had minimal impact on dust-holding capacity, demonstrating the method's robustness for rapid filter performance evaluation. RH strongly influenced loading, particularly for hygroscopic KCl aerosol, where elevated RH slowed loading by enhancing particle adhesion and increasing dust cake porosity. For electret filters, high RH further reduced filtration efficiency by accelerating charge decay on the filter media. Experimental repeatability was confirmed across replicate tests. This methodology provides a realistic, cost-effective, and time-efficient approach to evaluate HVAC filter aging, enabling improved performance assessments of filters in urban environments.

1. Introduction

People spend 70 % to 90 % of their time indoors, where exposure to airborne particles can negatively affect both physical and mental health [1–7]. Heating, ventilation, and air conditioning (HVAC) filters are a primary strategy for removing particles of outdoor and indoor origin in residential and commercial buildings [8]. Outdoor particles infiltrating indoor environments originate from both anthropogenic and biogenic sources, including vehicle tailpipe and non-tailpipe emissions, industrial emissions, construction activities, road dust resuspension, wildfire smoke emissions, secondary aerosol formation, sea spray aerosol generation, and biological material release of pollen grains, bacterial cells, and fungal spores [9–13]. Indoor particles arise from primary and secondary sources associated with occupants and their activities, including indoor combustion, cooking emissions, floor dust resuspension, cleaning activities, secondary aerosol formation, and emissions from electrical devices such as 3D and laser printers [14–22]. Research has also shown that HVAC filters can reduce indoor ozone levels by facilitating reactions between ozone and reactive material captured on the filter media [23, 24]. Historically, low-efficiency HVAC filters were primarily used to protect downstream equipment – such as fans and heat exchanger coils – from fouling due to coarse dust accumulation. However, growing awareness of occupant health has led to the widespread adoption of higher-efficiency air filters in HVAC systems. Given their extensive use in modern buildings, accurately evaluating HVAC filter performance is critical.

The performance of HVAC filters is governed by three key factors: airflow resistance, dust-holding capacity (DHC), and particle removal

* Corresponding author.
E-mail address: bboor@purdue.edu (B.E. Boor).

https://doi.org/10.1016/j.buildenv.2025.113564
Received 5 March 2025; Received in revised form 30 July 2025; Accepted 14 August 2025
Available online 14 August 2025

efficiency. While the primary function of air filters is to remove airborne particles, most studies emphasize particle removal efficiency, often neglecting the energy penalties associated with filter clogging. These energy penalties arise as accumulated particles increase airflow resistance (ΔP), forcing HVAC system fans to work harder to maintain volumetric airflow rates. Studies show that HVAC fans contribute to over 7 % of total building energy consumption [25]. Beyond electricity costs, filter maintenance represents a significant expense, as accelerated filter degradation leads to more frequent replacements, increased labor for installation, and disposal of used filters [26,27]. Filters are typically replaced once their ΔP reaches a predetermined threshold [28]. Consequently, filter ΔP directly impacts HVAC fan energy consumption while indirectly affecting operational costs related to filter procurement and labor. A more precise evaluation of the temporal evolution in HVAC filter airflow resistance can improve cost predictions and optimize HVAC filter management strategies.

Both experimental and modeling approaches have been used to assess changes in the airflow resistance of HVAC filters. For example, Feng et al. [29] applied computational fluid dynamics (CFD) to evaluate the ΔP of pleated filters, providing insights into airflow resistance for new, unaged filters. Similarly, Abam et al. [30] modeled ΔP across a 3D filter housing using CFD, offering valuable information on airflow dynamics through filters. While these studies enhance understanding of filter performance, they do not account for dust loading, which significantly impacts ΔP over time. As particles deposit and accumulate on filter media, filter properties evolve, influencing both airflow resistance and HVAC fan energy consumption. The impact of increasing filter ΔP depends on the HVAC fan type and its control strategy for motor speed and runtime [25,31–35]. In constant-speed fans, a higher filter ΔP can reduce energy use by lowering volumetric airflow rates, whereas in constant-airflow systems, it increases energy demand as the fan compensates for the added airflow resistance. Evaluating the temporal progression of filter ΔP is therefore essential for understanding long-term HVAC energy performance. Leung et al. [36] demonstrated the evolution of filter ΔP under continuous submicron aerosol loading and developed a predictive theoretical model. While modeling provides valuable insights into filter loading behavior, many studies focus on filter media sheets rather than full-scale HVAC filters or depth filtration of submicron particles, due to computational complexity [37–40]. Experimental research on HVAC filter loading under real-world conditions remains essential to complement modeling efforts and improve predictions of HVAC filter performance over time.

Experimental studies have shown that HVAC filter ΔP evolves differently in real-world conditions compared to laboratory settings [41,42]. This discrepancy largely stems from the loading dust used in laboratory evaluations, which does not accurately reflect the properties of airborne particles encountered in the field. In particular, the particle size distributions (PSDs) of loading dust often differ from those in urban atmospheric environments [43]. The impact of loading dust PSDs on ΔP has been widely studied [44–56], demonstrating that filters age differently when exposed to submicron particles (≤1 μm) versus coarse particles (>1 μm). Many studies report a more rapid filter ΔP increase with fine particles due to the formation of denser filter cakes, whereas coarser dusts tend to create more porous structures [50,51,55]. However, some studies suggest that larger particles can also accelerate filter loading under certain conditions. Despite these differing conclusions, particle size remains a key factor influencing HVAC filter performance. Current standards such as ANSI/ASHRAE Standard 52.2-2017, ISO 16890-1:2016, and ISO 29461-1:2021 primarily use coarse test dusts with geometric mean diameters greater than 1 μm to age HVAC filters, despite real-world urban and indoor aerosol PSDs being dominated by submicron particles on a number basis. This mismatch contributes to the differences in ΔP evolution observed between laboratory and field conditions. Although methods exist for generating submicron particles, a major challenge has been producing these particles at sufficiently high mass concentrations for rapid, full-scale HVAC filter loading tests [57]. Overcoming this limitation is critical for improving the relevance of laboratory filter testing to real-world scenarios.

High mass concentrations of loading dust are commonly used in laboratory settings to accelerate HVAC filter aging and simulate long-term performance within a short timeframe. However, studies have shown that high concentrations of coarse dust can significantly overestimate filter loading performance [48,58,59]. At elevated mass concentrations, coarse particles deposited on the filter surface lack

Fig. 1. Photographs of the full-scale HVAC filter test rig and TAG, including: (a) side-view of the full-scale HVAC filter test rig with the airflow direction right to left; (b) steam humidifier injection port; (c) steam humidifier; (d) aerosol sampling and measurement equipment, including the aerosol sampling tubes, solenoid valve, double ejector dilutors, flow splitter, SMPS, and HR-ELPI+; (e) TAG and salt aerosol injection port; and (f) pitot-tube array.

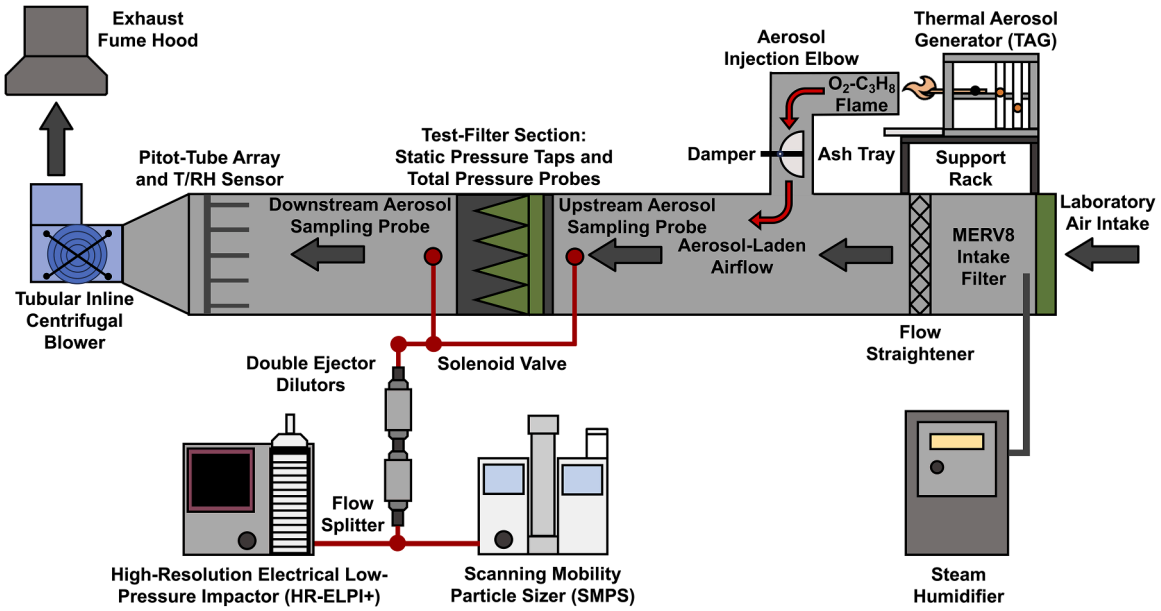

Fig. 2. Schematic of the full-scale HVAC filter test rig.

sufficient time and space to form a stable structure, resulting in a loose microstructure. This leads to a lower filter ΔP at the same loaded mass, artificially increasing the apparent DHC compared to real-world conditions with lower particle concentrations. In contrast, the impact of the mass concentration on HVAC filter loading curves is less pronounced when fine (≤1 μm) or ultrafine (≤0.1 μm) particles are used, as they require less time and space to stabilize on the filter surface, thereby minimizing the influence of particle concentrations on filter loading behavior. These findings underscore the need for improved HVAC filter loading procedures that better represent long-term performance by incorporating fine and ultrafine particles rather than the coarse dusts used in current standardized testing protocols. This adjustment would enhance the accuracy of HVAC filter performance evaluations under realistic operating conditions.

This study employed a novel high-concentration submicron aerosol generation technique – the thermal aerosol generator (TAG) – integrated into a full-scale HVAC filter test rig. The TAG produces higher mass concentrations of submicron salt aerosol than other existing aerosol generation methods [60,61], and its successful integration with the test rig has been validated in prior research [60,62]. Using this methodology, the aging performance of full-scale HVAC filters was evaluated and is reported here. Beyond the number and mass PSDs of the loading aerosol, several factors significantly influence the evolution of filter ΔP, including volumetric airflow rates [63–65], loading aerosol feed rates [48,59,60], and environmental conditions such as relative humidity (RH) [66–68]. The HVAC filter aging procedure in this study incorporated sensitivity tests to assess the effects of these conditions on filter loading curves (e.g. ΔP vs. loading time and ΔP vs. generated aerosol mass). Specifically, tests examined different airflow rates, salt aerosol mass production rates, and RH levels. Temperature effects were excluded, as previous research has shown minimal impact on filter loading performance and filter lifespan [68,69].

The objective of this study is to utilize synthetic high-mass-concentration submicron salt aerosol to rapidly age full-scale HVAC filters, enabling the evaluation of the temporal evolution of airflow resistance (ΔP) and its impact on HVAC system energy consumption when operated with a variable-frequency blower at a constant airflow rate. The generated aerosol was designed to exhibit PSDs representative of urban and indoor particulate matter, ensuring a realistic simulation of real-world HVAC filter applications. Sensitivity tests were conducted under various aging conditions to assess their influence on filter loading performance, simulating a range of operational environments HVAC filters may encounter. The resulting filter loading curves provide valuable insights into fan energy consumption and operational costs associated with HVAC filter performance over time. This work, as part of ASHRAE RP-1734, will contribute to the development of the forthcoming ASHRAE Guideline 35, *Method for Determining the Energy Consumption Caused by Air-Cleaning and Filtration Devices*.

2. Materials and methods

2.1. Full-scale HVAC filter test rig

The thermal aerosol generator (TAG) (Type 6000, SFP Services Ltd., Christchurch, UK) employs a high-temperature oxygen (O_2)-propane (C_3H_8) flame to burn salt sticks for generating submicron aerosol (Fig. 1). The salt sticks primarily consist of sodium chloride (NaCl) or potassium chloride (KCl), with a small amount of magnesium oxide (MgO) added as a binder. MgO does not vaporize but falls as hot ash. In this study, KCl-based salt sticks (10 mm diameter, 100 mm length) were used, with an effective KCl content of 0.1–0.13 g mm^{-1}, as specified by the manufacturer. The TAG continuously feeds salt sticks into the O_2-C_3H_8 flame at a fixed feed rate, ensuring the steady generation of submicron KCl aerosol at high mass concentrations. A detailed description of the TAG can be found in prior studies [60,62].

A custom-designed test rig was constructed to integrate the TAG as an aerosol source for HVAC filter aging (Figs. 1 and 2). The test rig includes a flow straightener, steam humidifier, steam humidifier injection port, a test-filter installation section, static pressure taps and total pressure probes connected to digital transducers for measuring the filter ΔP, a pitot-tube array for airflow measurement, and a high-capacity tubular inline centrifugal blower. The duct configuration follows ANSI/ASHRAE Standard 52.2–2017 specifications, with modifications to accommodate the TAG. The test rig simulates full-scale HVAC ductwork with a 24 × 24-in cross-sectional area and a 28-ft length. Additional details on the test rig design and integration with the TAG are available in a prior study [62].

Three minimum efficiency reporting value (MERV)-rated filters – MERV8, MERV13, and MERV14 – were tested in accordance with ASHRAE RP-1734 to support the development of the forthcoming ASHRAE Guideline 35. All had a nominal cross-sectional area of 24 × 24-in but varied in thickness and configuration. The MERV8 filters were

Table 1
Specifications of the HVAC filters evaluated in this study.

Filter Type	Filter Configuration	Nominal Size (HxWxD) (in)	Filter Media Area (ft^2)	Media Type	Electret Filter?
MERV8	Pleated Panel Filter	24 × 24 × 2	17.3	Synthetic Blend of Polyester Media	No
MERV13	Multi-Pocket Bag Filter	24 × 24 × 30	81	Blend of Synthetic Microfibers	Yes
MERV14	Mini-Pleated V-Bank Box Filter	24 × 24 × 12	200	Microfine Glass Fibers with an Acrylic Resin Binder	No

2-in pleated panel filters made from a proprietary fiber blend that relied solely on mechanical particle capture. The MERV13 filters were bag filters with eight 30-in-deep pockets, composed of electrostatically enhanced synthetic microfibers. The MERV14 filters were 12-in-deep mini-pleated V-bank box filters using microfine glass fiber media (Table 1).

2.2. Experimental protocol

A total of n=63 full-scale HVAC filter loading experiments were conducted under varying HVAC system operational and environmental conditions, categorized into four test groups for each filter type (Table 2): (1) baseline tests, (2) volumetric airflow rate sensitivity tests, (3) salt stick feed rate sensitivity tests, and (4) RH sensitivity tests. To assess repeatability, five replicates were conducted for each filter type in the baseline tests, while triplicate tests were performed for each sensitivity test category. A schematic representation of the experimental protocol is provided in Fig. 3.

Before each loading experiment, gravimetric measurements were taken to record the initial mass of the test-filter and salt sticks. An ash tray was placed in front of the TAG to collect MgO ash, with its empty mass recorded beforehand. After these measurements, the test-filter was installed in the filter bank, and painter's tape was applied around the edges to minimize airflow bypass. The exterior cover panel was reinstalled, and insulation foam was placed around it to ensure airtight conditions.

Following installation, the blower was activated, and motor frequency was regulated using a proportional-integral-derivative (PID) controller in LabVIEW (National Instruments Inc., Austin, TX, USA). The controller optimized blower speed in real-time to maintain a consistent in-duct volumetric airflow rate. Once the airflow stabilized, the TAG was ignited to generate submicron KCl aerosol, marking the start of the loading experiment. The experiment continued until the filter ΔP reached 1.5 in H_2O, as specified in ASHRAE RP-1734 to support the forthcoming ASHRAE Guideline 35 [70]. This endpoint aligns with prior studies, where a final ΔP approximately four to five times greater than the clean-filter ΔP is considered representative of HVAC filter service life [56,67,71,72].

Throughout the experiment, key operational parameters were manually recorded to ensure data integrity. Gas pressures (O_2 and C_3H_8) were checked every 20 min to verify a stable TAG gas supply. The PSD of the generated KCl aerosol was continuously monitored, with deviations in PSD shape serving as indicators of potential TAG malfunctions requiring immediate troubleshooting. These deviations typically occurred when (1) the salt stick was depleted and needed replacement or (2) the feeding mechanism became obstructed, disrupting aerosol generation. Manual intervention was required in both cases. Once the test-filter ΔP reached 1.5 in H_2O, the experiment was concluded. The TAG, blower, and steam humidifier were powered off, and the test-filter was carefully removed for final gravimetric measurement. The increase in filter mass was assumed to represent the total loaded aerosol mass, e.g., DHC. Additionally, the ash tray containing residual MgO ash was weighed to determine the total salt stick mass consumed, ensuring accurate accounting of aerosol generation.

2.3. Instrumentation and measurements

2.3.1. Aerosol instrumentation

Number-based PSDs of the synthetic submicron KCl aerosol were measured throughout each loading experiment. Two aerosol instruments were integrated into the test rig: (1) a scanning mobility particle sizer (SMPS) (Model 3938NL88, TSI Inc., Shoreview, MN, USA) with a long differential mobility analyzer (DMA) and (2) a high-resolution electrical low-pressure impactor (HR-ELPI+) (Dekati Ltd., Kangasala, Finland) with oil-soaked sintered collection plates (Figs. 1 and 2, Table 3). The SMPS measured electrical mobility diameter (D_{em})-based number PSDs ($dN/dLogD_{em}$, cm^{-3}) from D_{em} = 20.1–1000 nm with a 4-min scan interval, while the HR-ELPI+ measured aerodynamic

Table 2
Summary of baseline and sensitivity loading conditions and experimental matrix.

Experiment Type	Volumetric Airflow Rate [$ft^3\ min^{-1}$]	RH [%]	Salt Stick Feed Rate [$mm\ min^{-1}$]	Number of Experiments Per Filter Type	Filter Type
Baseline Experiments	2000	42.5 ± 2.5	10	5	MERV14 MERV13 MERV8
Volumetric Airflow Rate Sensitivity Experiments	1000	42.5 ± 2.5	10	3	MERV14 MERV13 MERV8
	500			3	MERV14 MERV13 MERV8
Salt Stick Feed Rate Sensitivity Experiments	2000	42.5 ± 2.5	18	3	MERV14 MERV13 MERV8
			5	3	MERV14 MERV13 MERV8
RH Sensitivity Experiments	2000	27.5 ± 2.5	10	3	MERV14
		57.5 ± 2.5		3	MERV14 MERV13 MERV8

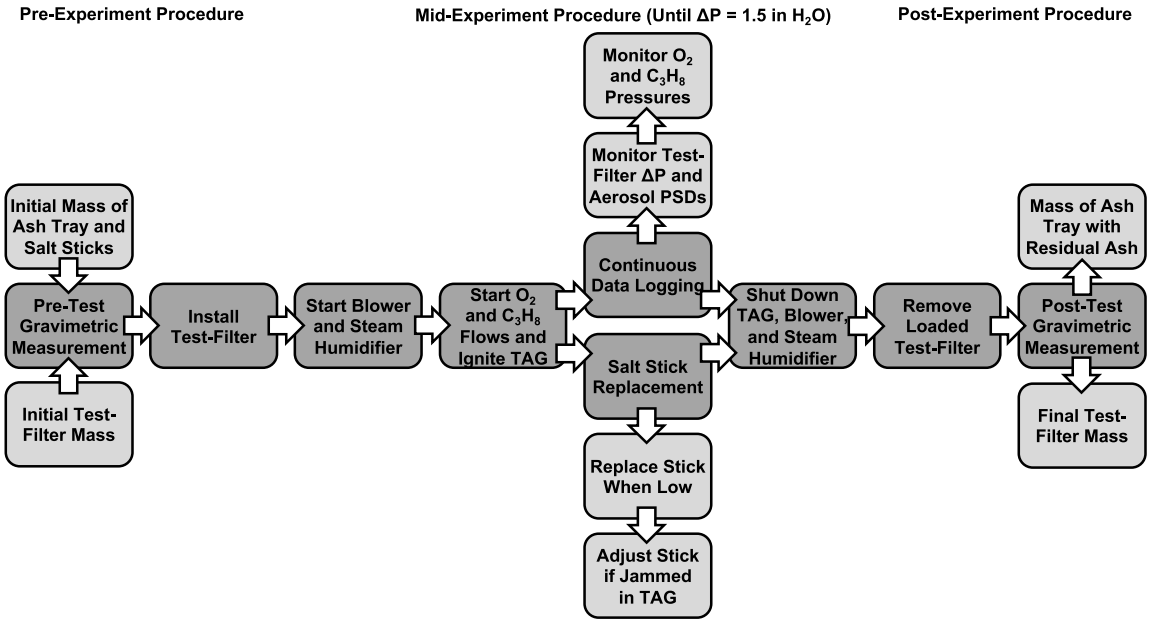

Fig. 3. Experimental protocol for the HVAC filter loading experiments.

Table 3
Description of instrumentation used in the HVAC filter test rig.

Instrument	Manufacturer	Model	Accuracy	Range	Function
Pressure Transducers	Setra Systems Inc.	Model 276	±0.25%	600 to 1100 mb	Barometric pressure measurement
		Model 265	±0.25%	0 to 5 in H_2O	Differential pressure transducer for filter airflow resistance measurement
			±0.25%	0 to 0.5 in H_2O	Differential pressure transducer for airflow rate measurement
Temperature & RH Transmitter	Setra Systems Inc.	Model SRH200	±2.5% RH ±0.3 °C	0 to 100% RH -40 to 60 °C	Sensor for monitoring in-duct temperature and RH
Pitot-Tubes	Dwyer Instruments LLC	Model 160	±2–5%	400 to 20,000 ft min^{-1}	Airflow velocity measurement
Data Acquisition Board	National Instruments Inc.	Model 6211	±2.69 mV	AO/I: ±10 *V*	Data acquisition for voltage signals and control
HR-ELPI+	Dekati Ltd.	–	–	6 to 10,000 nm	Aerosol number-based PSD measurement
SMPS	TSI Inc.	Model 3938NL88	–	20.1 to 1000 nm with long DMA	Aerosol number-based PSD measurement
Combustion Gas Detector	General Tools Inc.	Model NGD269	±50 ppm	0 to 20,000 ppm	Monitoring of C_3H_8 leakage

diameter (D_a)-based number PSDs ($dN/dLogD_a$, cm^{-3}) from D_a = 6–10,000 nm at a 1 Hz sampling rate, providing real-time PSD data. The SMPS ensured high measurement stability, while the HR-ELPI+ captured second-by-second PSD fluctuations during each loading experiment, making it particularly useful for monitoring TAG operation. Additional details on the aerosol instruments and KCl aerosol characteristics are available in previous studies [60,62].

Aerosol sampling probes were positioned upstream and downstream of the test-filter within the test rig. The upstream probe, placed 1 ft from the test-filter, minimized interference with the loading process, while the downstream probe, located 12 ft away, ensured aerosol mixing for uniform sampling. Both probes were centrally aligned within the duct for representative cross-sectional submicron aerosol measurements. The probes connected to sampling tubes beneath the test rig, which merged into a single outlet leading to the aerosol instruments (Figs. 1 and 2). A solenoid valve at the convergence point alternated sampling between upstream and downstream locations.

To handle high aerosol concentrations, a double dilutor system was employed, consisting of two ejector dilutors (DI-1000, Dekati Ltd., Kangasala, Finland) connected in series to achieve a high dilution factor. The diluted aerosol samples were directed into a four-way flow splitter (Model 1104, Brechtel Manufacturing Inc., Hayward, CA, USA), with two outlets connected to the SMPS and HR-ELPI+, while the other two remained open to ambient air to maintain pressure equilibrium (Figs. 1 and 2). Digital pressure transducers (Model 265, Setra Systems Inc., Boxborough, MA, USA) continuously monitored pressure differentials across each dilutor, and dilution factors were calculated using manufacturer calibration curves.

The raw SMPS and HR-ELPI+ data were processed by applying corrections for deposition losses in the sampling lines and accounting for dilution factors. Measured SMPS number-based PSDs were converted into estimated mass-based PSDs ($dM/dLogD_{em}$, μg m^{-3}) using the bulk density of KCl (ρ_p = 1.98 g cm^{-3}) and assuming a spherical particle morphology, as reported in a previous study [60].

2.3.2. HVAC filter pressure drop measurement

Both static pressure taps and total pressure probes were used to ensure reliable measurements of test-filter ΔP. Each method has distinct advantages and limitations, which should be considered when selecting an installation approach. Static pressure is influenced by airflow velocity, as total pressure is the sum of static and velocity pressure (Eq. 1). To accurately measure filter ΔP, the downstream static pressure tap must be positioned at a sufficient distance from the test-filter to allow the airflow velocity to recover. Immediately downstream of the filter, airflow velocity increases due to the reduced effective cross-sectional area, leading to a temporary drop in static pressure. Without adequate

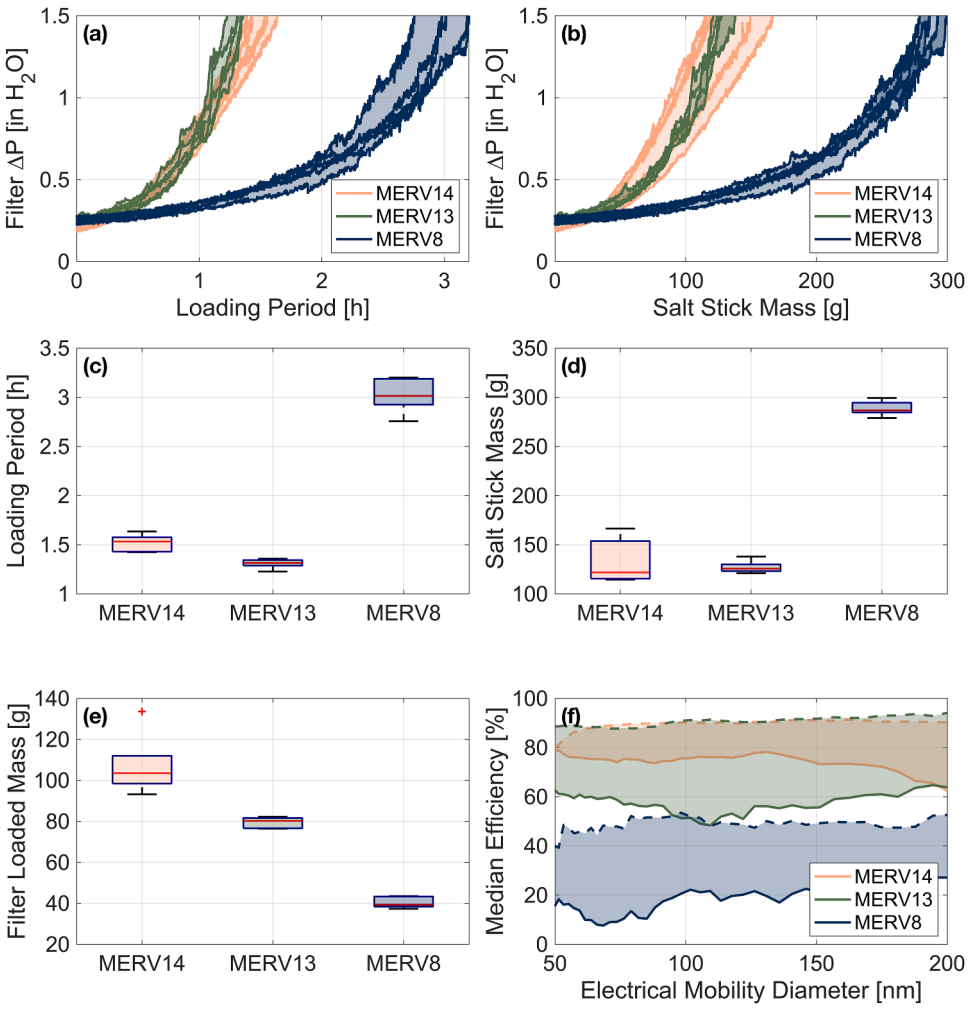

Fig. 4. Time-series plots (a, b), box plots (c to e), and filtration efficiency curves (f) of the submicron particle loading kinetics for different types of test-filters (pink color for MERV14, green color for MERV13, and blue color for MERV8): (a) test-filter ΔP vs. loading period; (b) test-filter ΔP vs. the mass of salt sticks consumed by the TAG during the entire loading period; (c) summarized loading period for each type of test-filter; (d) summarized mass of salt sticks consumed for each type of test-filter; (e) change in the test-filter mass (loaded filter mass – initial filter mass) for each type of test-filter; (f) median initial filtration efficiency (solid line) and the final efficiency (dashed line). The time-series plots illustrate the real-time measurement of the test-filter ΔP at 1 Hz with five curves for each type of test-filter, each curve indicating an individual experiment at the baseline loading condition and the shaded area showing the range that the replicate experiments enclosed. The box plots illustrate the median value (red line) and the interquartile range from the 25th to 75th percentile (blue box). The whiskers indicate the range of the remaining data, excluding outliers, which are plotted individually as red plus signs.

recovery distance, downstream static pressure may be underestimated [29].

In contrast, total pressure probes measure the combined effects of velocity and static pressure, making them less affected by localized velocity increases at the filter exit. This allows for more flexible probe placement. In this study, downstream static pressure taps were positioned 2 ft from the test-filter, while upstream static pressure taps and total pressure probes were located 1 ft upstream. Downstream total pressure probes were installed 1 ft downstream of the test-filter.

$$P_{total} = P_{velocity} + P_{static} \tag{1}$$

To further improve measurement accuracy, four static pressure taps were installed on each side of the test rig wall, while four total pressure probes were placed at varying heights along the diagonal of the test rig's cross-sectional area. The taps and probes were connected via four equal-length nylon tubes, which merged into a single tube leading to the pressure transducers (Model 265, Setra Systems Inc., Boxborough, MA, USA) (Table 3). This setup ensured the transducer recorded an averaged pressure value, improving the reliability of the filter ΔP measurements.

2.3.3. Volumetric airflow rate measurement

Pitot-tubes were installed downstream of the test-filter to measure the in-duct volumetric airflow rate. This location was selected to minimize turbulence, ensuring more stable and reliable measurements. Pitot-tubes measure both static and total pressure, allowing velocity pressure to be determined by subtracting static pressure from total pressure. The airflow velocity is then calculated using Eq. (2) and converted to a volumetric airflow rate by multiplying by the test rig's cross-sectional area.

$$u = \sqrt{2 \times \frac{P_{total} - P_{static}}{\rho}} \tag{2}$$

Where u is airflow velocity, and ρ is air density. Assuming ideal gas behavior, air density is a function of absolute temperature and pressure. A barometric pressure meter measured ambient atmospheric pressure (Model 276, Setra Systems Inc., Boxborough, MA, USA), while a T/RH transmitter (Model SRH200, Setra Systems Inc., Boxborough, MA, USA) inside the test rig monitored in-duct temperature and RH (Table 3). These measurements were used to calculate air density for airflow

Table 4
Summary of HVAC filter loading performance across different baseline and sensitivity tests.

	Filter Type	Conditions for Baseline and Sensitivity Experiments	Loading Period [h]: Mean ± Std	Salt Stick Mass Consumption [g]:		Filter Loaded Mass [g]:	
				Mean ± Std	COV	Mean ± Std	COV
Impact of Filter Type	MERV14	Baseline Conditions	1.5 ± 0.06	133.6 ± 23	42.9 %	107 ± 15.5	39.1 %
	MERV13	Baseline Conditions	1.3 ± 0.05	127.2 ± 6.4		79.4 ± 2.7	
	MERV8	Baseline Conditions	3.0 ± 0.18	288.8 ± 7.7		40.4 ± 2.8	
Impact of Volumetric Airflow Rate	MERV14	2000 ft^3 min^{-1} (Baseline)	1.5 ± 0.06	133.6 ± 23	27.9 %	107 ± 15.5	25.2 %
		1000 ft^3 min^{-1}	2.34 ± 0.08	218 ± 22		159 ± 18	
		500 ft^3 min^{-1}	2.8 ± 0.1	228 ± 20		177 ± 12	
	MERV13	2000 ft^3 min^{-1} (Baseline)	1.3 ± 0.05	127.2 ± 6.4	5.0 %	79.4 ± 2.7	10.3 %
		1000 ft^3 min^{-1}	1.3 ± 0.13	136.8 ± 3		99.2 ± 2.7	
		500 ft^3 min^{-1}	1.3 ± 0.04	126.1 ± 2.3		87.6 ± 3	
	MERV8	2000 ft^3 min^{-1} (Baseline)	3.0 ± 0.18	288.8 ± 7.7	18.0 %	40.4 ± 2.8	11.3 %
		1000 ft^3 min^{-1}	4.03 ± 0.3	363.9 ± 52.9		47.9 ± 3.7	
		500 ft^3 min^{-1}	4.4 ± 0.5	413.9 ± 27.2		49.2 ± 2.6	
Impact of Salt Stick Feed Rate	MERV14	18 mm min^{-1}	1.03 ± 0.02	133 ± 9	12.4 %	92 ± 24	16.2 %
		10 mm min^{-1} (Baseline)	1.5 ± 0.06	133.6 ± 23		107 ± 15.5	
		5 mm min^{-1}	3.1 ± 0.1	150 ± 2		113 ± 4	
	MERV13	18 mm min^{-1}	0.8 ± 0.04	125.3 ± 2	5.5 %	76.8 ± 4	4.2 %
		10 mm min^{-1} (Baseline)	1.3 ± 0.05	127.2 ± 6.4		79.4 ± 2.7	
		5 mm min^{-1}	2.37 ± 0.07	119 ± 9.6		75.6 ± 2.7	
	MERV8	18 mm min^{-1}	2.3 ± 0.43	307.9 ± 50.1	17.7 %	41.1 ± 7	10.1 %
		10 mm min^{-1} (Baseline)	3.0 ± 0.18	288.8 ± 7.7		40.4 ± 2.8	
		5 mm min^{-1}	7.9 ± 0.32	405 ± 27.3		37.5 ± 2.6	
Impact of RH	MERV14	57.5 ± 2.5 % RH	3.6 ± 0.13	309.7 ± 7	54.9 %	225 ± 5.5	50.6 %
		42.5 ± 2.5 % RH (Baseline)	1.5 ± 0.06	133.6 ± 23		107 ± 15.5	
		27.5 ± 2.5 % RH	0.91 ± 0.02	91 ± 21		68.4 ± 10	
	MERV13	57.5 ± 2.5 % RH	5.1 ± 0.2	450 ± 32.6	67.7 %	210.8 ± 3.6	52.9 %
		42.5 ± 2.5 % RH (Baseline)	1.3 ± 0.05	127.2 ± 6.4		79.4 ± 2.7	
	MERV8	57.5 ± 2.5 % RH	8.9 ± 1.34	805.2 ± 110	56.7 %	87.4 ± 12.6	43.6 %
		42.5 ± 2.5 % RH (Baseline)	3.0 ± 0.18	288.8 ± 7.7		40.4 ± 2.8	

velocity determination.

Following ANSI/ASHRAE Standard 41.2–2022 recommendations [73], a self-averaging pitot-tube array was designed to measure mean airflow velocity along the diagonal of the test rig's cross-section. The array included five pitot-tubes (Model 160, Dwyer Instruments LLC, Michigan City, IN, USA), with their static pressure ports connected together and their total pressure ports similarly connected. The combined static pressure was routed to a single outlet connected to a pressure transducer (Model 265, Setra Systems Inc., Boxborough, MA, USA), and the same configuration was applied for the total pressure. Real-time volumetric airflow rate calculations were performed in LabVIEW, which also provided PID-controlled feedback to maintain a constant airflow rate. To prevent clogging, a self-cleaning system periodically purged pitot-tube orifices with particle-free compressed air. Two solenoid valves alternated between the compressed air source and the pressure transducer, automatically switching every 30 min for a 1-min purge before resuming normal operation. This cleaning process was integrated into LabVIEW and conducted without interrupting test rig operation.

2.4. HVAC filter performance evaluation metrics

The test-filter ΔP increased over time due to loading with the TAG-generated submicron KCl aerosol, with ΔP recorded at 1 Hz in LabVIEW. Two HVAC filter loading curves were analyzed: (1) real-time ΔP growth as a function of the loading time, starting from TAG ignition, and (2) ΔP growth as a function of the total salt stick mass consumed during the loading process. The volumetric airflow rate, in-duct temperature, and RH were recorded at 1 Hz to evaluate their influence on filter performance in sensitivity tests. The initial and final masses of test-filters were measured to determine the total loaded KCl aerosol mass, representing filter DHC. DHC is a key parameter linked to filter lifetime, making it a critical metric for assessing overall filter performance. Lastly, size-resolved filtration efficiency was calculated from the difference between upstream and downstream number-PSDs. Since upstream and downstream PSDs were not measured simultaneously, upstream concentrations were assumed to remain stable during sample valve switching.

3. Results and discussion

The following sections present the results of the artificial loading study using synthetic submicron KCl aerosol under various loading conditions. First, the impact of the HVAC filter type on loading performance is analyzed under baseline conditions (2000 ft^3 min^{-1} airflow rate; 10 mm min^{-1} salt stick feed rate; 42.5 ± 2.5 % RH). Next, airflow rate effects are examined across different settings (2000, 1000, and 500 ft^3 min^{-1} airflow rate; 10 mm min^{-1} salt stick feed rate; 42.5 ± 2.5 % RH). Additional sensitivity tests assess the influence of the salt stick feed rate (2000 ft^3 min^{-1} airflow rate; 18, 10, 5 mm min^{-1} salt stick feed rate; 42.5 ± 2.5 % RH) and RH (2000 ft^3 min^{-1} airflow rate; 10 mm min^{-1} salt stick feed rate; 57.5 ± 2.5 %, 42.5 ± 2.5 %, 27.5 ± 2.5 % RH) on filter loading performance. Filter loading performance is evaluated based on two primary metrics: (1) the loading period (in hours) required for the filter ΔP to increase from its initial value to the final ΔP = 1.5 in H_2O and (2) the total mass of salt sticks (in grams) consumed during loading, determined through gravimetric measurements after accounting for the mass of MgO ash. Additionally, the test-filter loaded mass is reported for each experiment to quantify DHC under varying conditions.

3.1. Impact of HVAC filter type on filter loading performance

HVAC filter type significantly influences loading duration, a key factor in assessing filter longevity and performance. Variations in filter media porosity and capture mechanisms affect loading behavior, as different filters exhibit distinct filtration efficiencies and changes in porosity over time. Fig. 4 presents the loading curves for each filter under baseline conditions (2000 ft^3 min^{-1} airflow rate; 10 mm min^{-1} salt stick feed rate; 42.5 ± 2.5 % RH). MERV14 and MERV13 filters had similar loading times to reach a final ΔP of 1.5 in H_2O, consuming comparable amounts of salt stick mass. Table 4 summarizes the mean (±

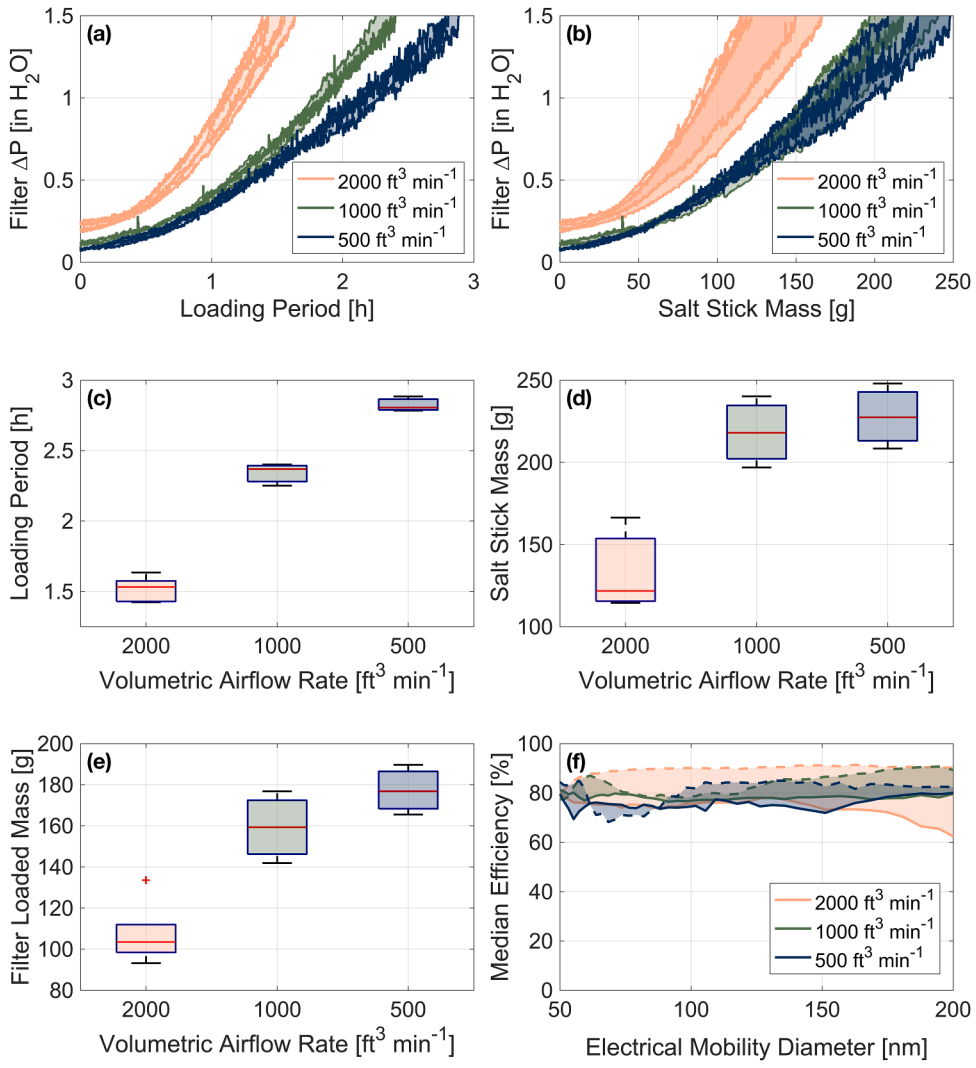

Fig. 5. Time-series plots (a, b), box plots (c to e), and filtration efficiency curves (f) of the submicron particle loading kinetics for MERV14 test-filters at different volumetric airflow rate setpoints (pink color for 2000 ft^3 min^{-1}, green color for 1000 ft^3 min^{-1}, and blue color for 500 ft^3 min^{-1}): (a) test-filter ΔP vs. loading period; (b) test-filter ΔP vs. the mass of salt sticks consumed by the TAG during the entire loading period; (c) summarized loading period for each airflow rate setpoint; (d) summarized mass of salt sticks consumed for each airflow rate setpoint; (e) change in the test-filter mass (loaded filter mass – initial filter mass) for each airflow rate setpoint; (f) median initial filtration efficiency (solid line) and the final efficiency (dashed line). The time-series plots illustrate the real-time measurement of the test-filter ΔP at 1 Hz with three or five curves for each airflow rate setpoint, each curve indicating an individual experiment at the airflow rate loading condition and the shaded area showing the range that the replicate experiments enclosed. The box plots illustrate the median value (red line) and the interquartile range from the 25th to 75th percentile (blue box). The whiskers indicate the range of the remaining data, excluding outliers, which are plotted individually as red plus signs.

standard deviation) loading period, total salt stick mass consumed, and test-filter loaded mass for each filter type and sensitivity test. The loading period for MERV14 and MERV13 was 1.5 ± 0.06 h and 1.3 ± 0.05 h, respectively. The salt stick mass consumed by the TAG for MERV14 and MERV13 test-filters was 133.6 ± 23 g and 127.2 ± 6.4 g, respectively. Filter loaded mass was 107 ± 15.5 g for MERV14 and 79.4 ± 2.7 g for MERV13. In contrast, MERV8 filters exhibited a significantly longer loading period (3.0 ± 0.18 h) and consumed more salt sticks (288.8 ± 7.7 g). Their loaded mass was 40.4 ± 2.8 g.

According to ANSI/ASHRAE Standard 52.2–2017, MERV14 filters must achieve at least 75 % efficiency for particles between 0.3 and 1.0 μm [70]. Their high efficiency enabled faster loading compared to MERV8 filters. These results align with previous studies showing that filters with higher MERV ratings (evaluated for particles ≥300 nm) also capture ultrafine particles (≤100 nm) more effectively [74,75]. The lower efficiency of MERV8 filters led to approximately double the loading time to reach the final ΔP of 1.5 in H_2O and higher salt stick consumption due to the prolonged loading process at the same salt stick feed rate. As a result, MERV8 filters had significantly lower loaded mass than MERV14 and MERV13 filters, underscoring the trade-off between filtration efficiency and operational longevity among different filters.

Contrary to expectations, MERV13 filters did not exhibit a longer loading period than MERV14 filters despite their lower efficiency rating. This discrepancy is likely due to differences in filtration mechanisms between mechanical and electret filters. MERV14 and MERV8 filters are mechanical filters, capturing particles via diffusion, interception, inertial impaction, and gravitational settling [76]. In contrast, MERV13 filters are electret filters, which use electrostatic forces – including Coulombic and dielectrophoretic attraction – alongside mechanical mechanisms to enhance particle capture efficiency [68,76–78].

The unique loading behavior of MERV13 filters may stem from the charging characteristics of the KCl aerosol generated by the TAG. The O_2-C_3H_8 flame used in the TAG is known to produce flame-induced ions through chemi-ionization [79], which can attach to KCl aerosol particles during their formation. Hydrocarbon flames, including O_2-C_3H_8 flames, generate ion concentrations ranging from 10^{10} to 10^{12} ions cm^{-3},

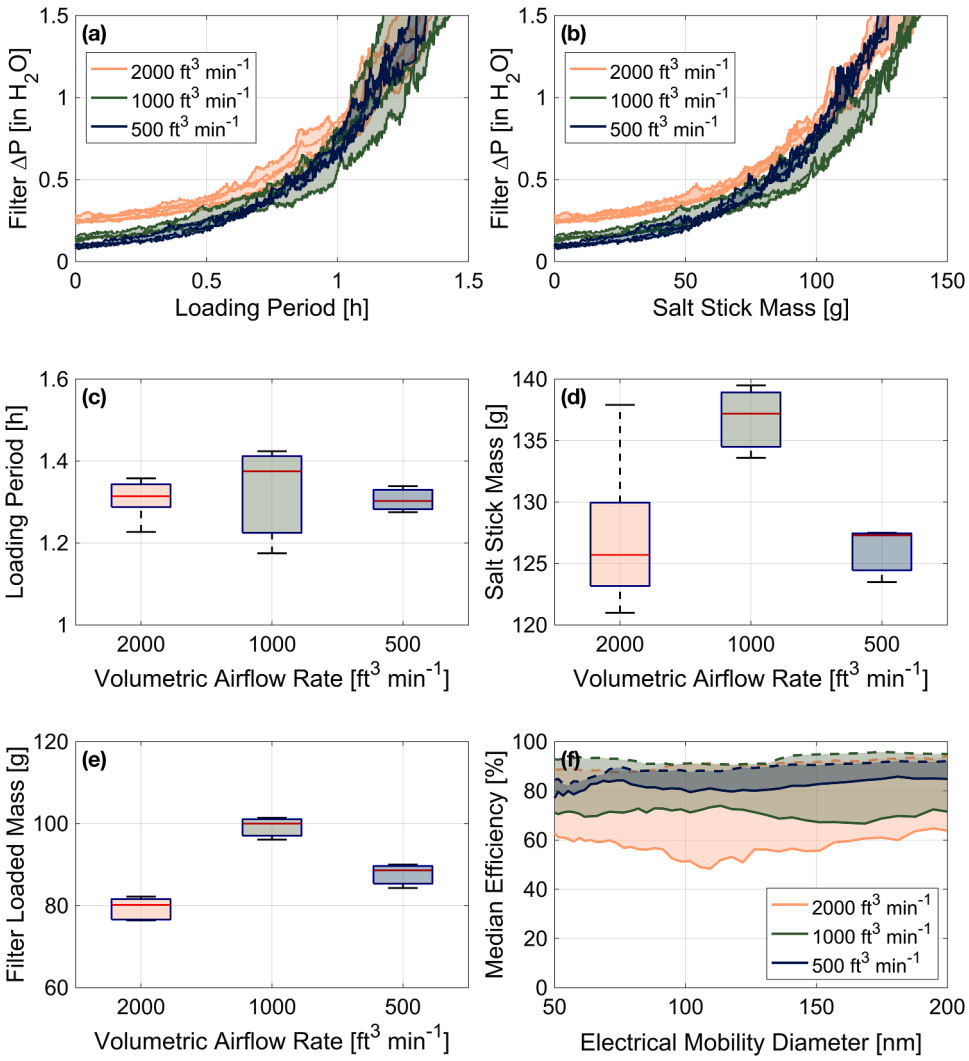

Fig. 6. Time-series plots (a, b), box plots (c to e), and filtration efficiency curves (f) of the submicron particle loading kinetics for MERV13 test-filters at different volumetric airflow rate setpoints (pink color for 2000 ft^3 min^{-1}, green color for 1000 ft^3 min^{-1}, and blue color for 500 ft^3 min^{-1}): (a) test-filter ΔP vs. loading period; (b) test-filter ΔP vs. the mass of salt sticks consumed by the TAG during the entire loading period; (c) summarized loading period for each airflow rate setpoint; (d) summarized mass of salt sticks consumed for each airflow rate setpoint; (e) change in the test-filter mass (loaded filter mass – initial filter mass) for each airflow rate setpoint; (f) median initial filtration efficiency (solid line) and the final efficiency (dashed line). The time-series plots illustrate the real-time measurement of the test-filter ΔP at 1 Hz with three or five curves for each airflow rate setpoint, each curve indicating an individual experiment at the airflow rate loading condition and the shaded area showing the range that the replicate experiments enclosed. The box plots illustrate the median value (red line) and the interquartile range from the 25th to 75th percentile (blue box). The whiskers indicate the range of the remaining data, excluding outliers, which are plotted individually as red plus signs.

consisting of positively charged species (e.g., CH_3^+, $C_3H_3^+$, CHO^+, CHO_2^+, CH_2O^+, H_3O^+) and negatively charged ions (e.g., HO_2^-, H_2O^-), as well as free electrons [79,80]. These ions can interact with aerosol particles in the flame, often leading to a dominant negative charge state due to higher electron attachment rates [81–84]. Preliminary measurements using the HR-ELPI+ (with its corona charger disabled) confirmed that the generated KCl aerosol exhibited bipolar charges across different particle sizes, consistent with charged aerosol characteristics.

Electret filters like MERV13 contain dielectric materials that develop quasi-permanent electrostatic charges when subject to an external charging process [85]. When capturing neutral particles, electret filters primarily rely on dielectrophoretic forces. However, when exposed to charged particles, Coulombic attraction and dielectrophoretic forces act synergistically, enhancing filtration efficiency [78,86,87]. Given the charged nature of the TAG-generated KCl aerosol, it is plausible that the electrostatic charge on the MERV13 filter media increased as loading progressed, further enhancing particle capture efficiency. This reinforcement of electrostatic forces could explain why MERV13 filters exhibited loading performance comparable to or exceeding that of mechanical MERV14 filters under these specific conditions. These findings align with previous studies indicating that electret filters perform better when exposed to charged aerosol [88].

3.2. *Impact of volumetric airflow rate on filter loading performance*

Fig. 5 presents the loading curves for MERV14 filters under varying airflow rates (2000, 1000, and 500 ft^3 min^{-1}). As summarized in Table 4, the baseline tests at 2000 ft^3 min^{-1} resulted in a loading period of 1.5 ± 0.06 h and consumed 133.6 ± 23 g of salt stick mass. At reduced airflow rates, the loading time increased to 2.34 ± 0.08 h at 1000 ft^3 min^{-1} (salt stick consumption: 218 ± 22 g) and 2.8 ± 0.1 h at 500 ft^3 min^{-1} (salt stick consumption: 228 ± 20 g). The corresponding filter loaded masses were 107 ± 15.5 g, 159 ± 18 g, and 177 ± 12 g for airflow rates of 2000, 1000, and 500 ft^3 min^{-1}, respectively. A clear trend emerges – lower airflow rates extend the loading period and increase salt stick consumption, indicating slower clogging at reduced velocities.

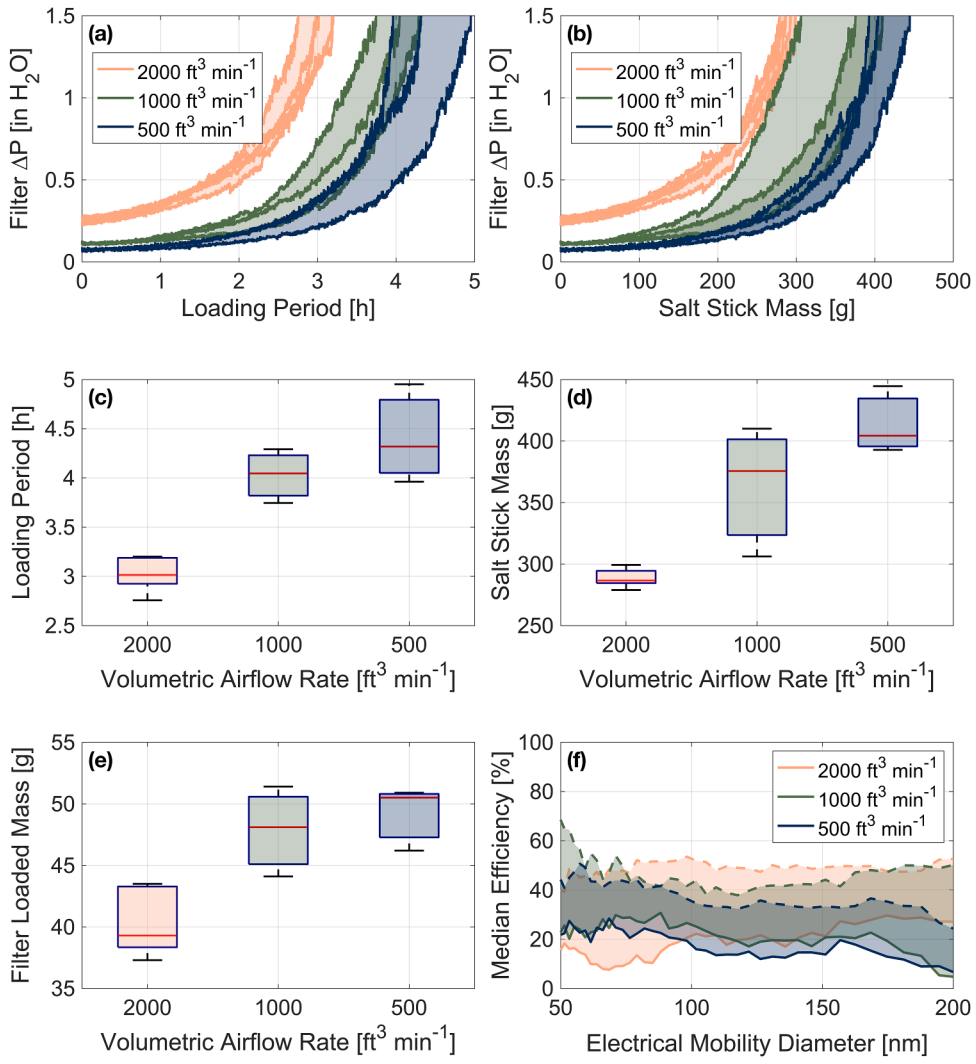

Fig. 7. Time-series plots (a, b), box plots (c to e), and filtration efficiency curves (f) of the submicron particle loading kinetics for MERV8 test-filters at different volumetric airflow rate setpoints (pink color for 2000 ft^3 min^{-1}, green color for 1000 ft^3 min^{-1}, and blue color for 500 ft^3 min^{-1}): (a) test-filter ΔP vs. loading period; (b) test-filter ΔP vs. the mass of salt sticks consumed by the TAG during the entire loading period; (c) summarized loading period for each airflow rate setpoint; (d) summarized mass of salt sticks consumed for each airflow rate setpoint; (e) change in the test-filter mass (loaded filter mass – initial filter mass) for each airflow rate setpoint; (f) median initial filtration efficiency (solid line) and the final efficiency (dashed line). The time-series plots illustrate the real-time measurement of the test-filter ΔP at 1 Hz with three or five curves for each airflow rate setpoint, each curve indicating an individual experiment at the airflow rate loading condition and the shaded area showing the range that the replicate experiments enclosed. The box plots illustrate the median value (red line) and the interquartile range from the 25th to 75th percentile (blue box). The whiskers indicate the range of the remaining data, excluding outliers, which are plotted individually as red plus signs.

Additionally, the initial filter ΔP was lower at reduced airflow rates, contributing to longer loading durations. These results align with prior studies demonstrating that ΔP is directly proportional to airflow rate, as predicted by theoretical and empirical models [56,63,64,71,89–94].

Modeling studies have shown that for clean filters, ΔP is influenced by airflow properties (e.g., viscosity, velocity) and filter characteristics such as fiber diameter and packing density. At higher airflow velocities, increased friction and turbulence elevate ΔP. As filters accumulate particles, both filter porosity and dust cake porosity decrease, further increasing resistance to airflow. Lower airflow rates mitigate these effects by slowing clogging dynamics and reducing initial ΔP, extending filter lifespan while requiring greater salt stick consumption to reach the final ΔP threshold [56,63,64,71,89–94].

Fig. 6 shows the loading curves for MERV13 filters under the same airflow rate conditions. Baseline tests at 2000 ft^3 min^{-1} resulted in a loading period of 1.3 ± 0.05 h and consumed 127.2 ± 6.4 g of salt stick mass. At 1000 ft^3 min^{-1}, the loading period was 1.3 ± 0.13 h (salt stick consumption: 136.8 ± 3 g), while at 500 ft^3 min^{-1}, the loading time was 1.3 ± 0.04 h (salt stick consumption: 126.1 ± 2.3 g). The corresponding filter loaded masses were 79.4 ± 2.7 g, 99.2 ± 2.7 g, and 87.6 ± 3 g for airflow rates of 2000, 1000, and 500 ft^3 min^{-1}, respectively. While the initial ΔP decreased with airflow rate, MERV13 filters exhibited similar loading periods and salt stick consumption across all airflow rates. This behavior likely stems from their electrostatic filtration mechanism, which enhances particle capture at lower airflow rates, unlike mechanical filters such as MERV14 and MERV8.

A comparison of initial filtration efficiencies showed that MERV13 filters captured more 50–200 nm particles at 500 ft^3 min^{-1} than at 1000 or 2000 ft^3 min^{-1}. The increased efficiency at lower airflow rates is due to longer particle retention times within the filter media, allowing more opportunities for charged particles to be captured by electrostatic forces [95,96]. This effect is particularly pronounced for submicron KCl aerosol, where Coulombic attraction and dielectrophoretic forces dominate over mechanical filtration. The higher initial filtration efficiency of MERV13 filters at 500 ft^3 min^{-1} facilitated faster depth filtration and dust cake formation, reducing media porosity and accelerating

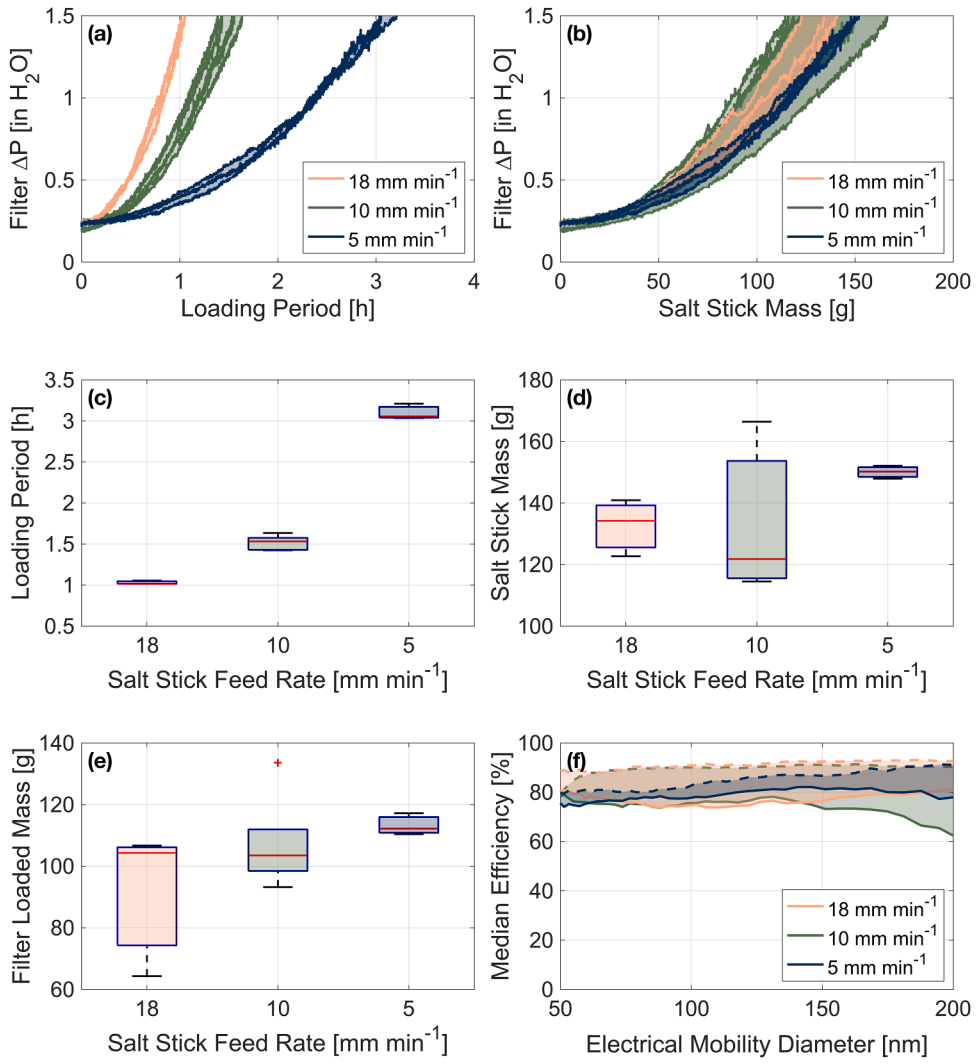

Fig. 8. Time-series plots (a, b), box plots (c to e), and filtration efficiency curves (f) of the submicron particle loading kinetics for MERV14 test-filters at different salt stick feed rate setpoints (pink color for 18 mm min^{-1}, green color for 10 mm min^{-1}, and blue color for 5 mm min^{-1}): (a) test-filter ΔP vs. loading period; (b) test-filter ΔP vs. the mass of salt sticks consumed by the TAG during the entire loading period; (c) summarized loading period for each salt stick feed rate setpoint; (d) summarized mass of salt sticks consumed for each salt stick feed rate setpoint; (e) change in the test-filter mass (loaded filter mass – initial filter mass) for each salt stick feed rate setpoint; (f) median initial filtration efficiency (solid line) and the final efficiency (dashed line). The time-series plots illustrate the real-time measurement of the test-filter ΔP at 1 Hz with three or five curves for each salt stick feed rate setpoint, each curve indicating an individual experiment at the salt stick feed rate loading condition and the shaded area showing the range that the replicate experiments enclosed. The box plots illustrate the median value (red line) and the interquartile range from the 25th to 75th percentile (blue box). The whiskers indicate the range of the remaining data, excluding outliers, which are plotted individually as red plus signs.

ΔP evolution. Consequently, the electret-enhanced filtration efficiency counterbalanced the effects of lower airflow velocity, explaining the similar loading durations across all tested airflow rates for MERV13 filters.

Fig. 7 presents the airflow rate sensitivity curves for MERV8 filters. The baseline tests at 2000 ft^3 min^{-1} resulted in a loading period of 3.0 ± 0.18 h and consumed 288.8 ± 7.7 g of salt stick mass. At 1000 ft^3 min^{-1}, the loading time increased to 4.03 ± 0.3 h (salt stick consumption: 363.9 ± 52.9 g), while at 500 ft^3 min^{-1}, it reached 4.4 ± 0.5 h (salt stick consumption: 413.9 ± 27.2 g). The corresponding filter loaded masses were 40.4 ± 2.8 g, 47.9 ± 3.7 g, and 49.2 ± 2.6 g for airflow rates of 2000, 1000, and 500 ft^3 min^{-1}, respectively. MERV8 filters followed the same trend as MERV14 filters, with lower airflow rates prolonging the loading period and increasing salt stick consumption due to slower clogging dynamics. However, the total loaded mass remained notably lower than that of MERV14 filters, increasing only slightly at lower airflow rates. This difference is attributed to the lower filtration efficiency of MERV8 filters, which capture fewer particles, limiting mass accumulation despite extended loading durations.

Airflow rate also influenced the KCl aerosol PSDs, affecting filter loading performance. Lower airflow rates increased particle residence time, promoting coagulation and shifting PSDs toward larger particle sizes [62]. At 2000 ft^3 min^{-1}, the KCl aerosol peak diameter was D_{em} ~ 90 nm, while at 500 ft^3 min^{-1}, it increased to D_{em} ~ 110 nm. Prior studies indicate that finer particles accelerate filter ΔP evolution [44–48,53,67]. This aligns with the trends observed for mechanical filters (MERV8 and MERV14), where the higher 2000 ft^3 min^{-1} airflow rate resulted in number PSDs that shifted to smaller particles and faster ΔP growth. Consequently, PSD shifts due to varying airflow rates likely contributed to the observed differences in filter loading. Specifically, larger particle sizes at lower airflow rates may slow down filter clogging due to reduced penetration into the filter media and less pronounced depth filtration effects. This interaction underscores the complex interplay between PSDs, airflow rates, and filter performance.

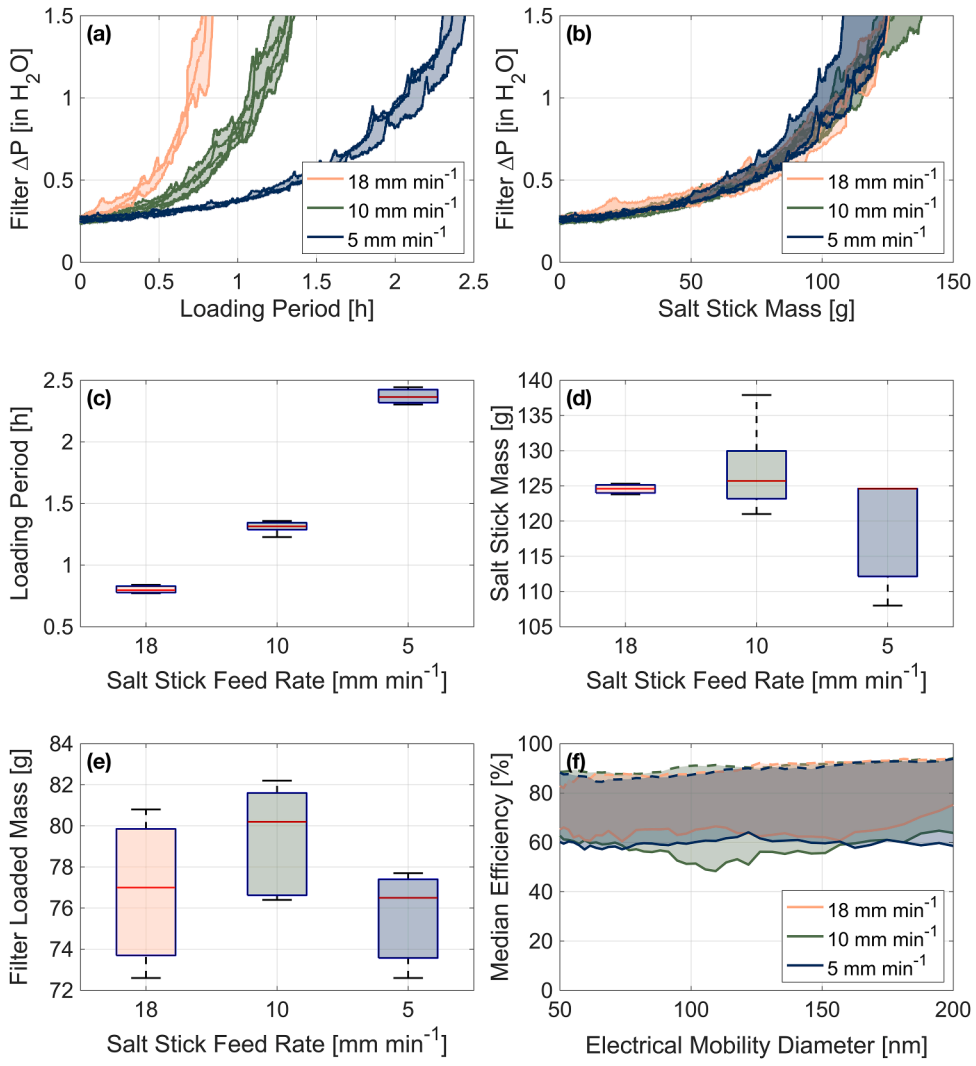

Fig. 9. Time-series plots (a, b), box plots (c to e), and filtration efficiency curves (f) of the submicron particle loading kinetics for MERV13 test-filters at different salt stick feed rate setpoints (pink color for 18 mm min^{-1}, green color for 10 mm min^{-1}, and blue color for 5 mm min^{-1}): (a) test-filter ΔP vs. loading period; (b) test-filter ΔP vs. the mass of salt sticks consumed by the TAG during the entire loading period; (c) summarized loading period for each salt stick feed rate setpoint; (d) summarized mass of salt sticks consumed for each salt stick feed rate setpoint; (e) change in the test-filter mass (loaded filter mass – initial filter mass) for each salt stick feed rate setpoint; (f) median initial filtration efficiency (solid line) and the final efficiency (dashed line). The time-series plots illustrate the real-time measurement of the test-filter ΔP at 1 Hz with three or five curves for each salt stick feed rate setpoint, each curve indicating an individual experiment at the salt stick feed rate loading condition and the shaded area showing the range that the replicate experiments enclosed. The box plots illustrate the median value (red line) and the interquartile range from the 25th to 75th percentile (blue box). The whiskers indicate the range of the remaining data, excluding outliers, which are plotted individually as red plus signs.

3.3. *Impact of salt stick feed rate on filter loading performance*

Fig. 8 presents the loading behavior of MERV14 filters at different salt stick feed rates. At 18 mm min^{-1}, loading was completed in 1.03 ± 0.02 h, consuming 133 ± 9 g of salt stick mass, with a filter loaded mass of 92 ± 24 g. The baseline 10 mm min^{-1} feed rate resulted in a 1.5 ± 0.06 h loading time, consuming 133.6 ± 23 g, with a loaded mass of 107 ± 15.5 g. At the lowest feed rate (5 mm min^{-1}), the loading time increased to 3.1 ± 0.1 h, with 150 ± 2 g of salt stick mass consumed and a loaded mass of 113 ± 4 g (Table 4). Lower feed rates led to longer loading times and slower filter ΔP growth, but total salt stick consumption and filter loaded mass remained similar across all settings, with coefficients of variance (COV) for salt stick consumption and filter loaded mass of 12.4 % and 16.2 %, respectively. The COVs across different salt stick feed rates are significantly smaller than that of different airflow rates (27.9 % and 25.2 %) and RHs (54.9 % and 50.6 %) for MERV14 test-filters (Table 4). This indicates that while higher feed rates accelerate loading, the DHC remains relatively consistent. These findings validate the method's ability to rapidly age filters for long-term performance evaluation without introducing significant bias, unlike conventional testing with coarse dust at high mass concentrations [48,58,59].

Minor variations in filter loaded mass likely result from differences in deposition dynamics at higher feed rates, where rapid particle accumulation forms denser dust cakes. However, these effects were minimal due to the use of submicron particles. Prior studies have similarly shown that feed rate effects diminish as particle size decreases [48,59]. This is due to differences in filtration mechanisms – submicron particles penetrate deeper into the filter media, promoting depth filtration, whereas coarser particles accumulate on the surface. In depth filtration, loading curves remain consistent across feed rates as ultrafine particles require less time and space to integrate into the filter media compared to larger particles. Once surface filtration becomes dominant, similar loading trends are observed due to the rapid growth in filter ΔP associated with surface dust cake formation. This underscores the reduced

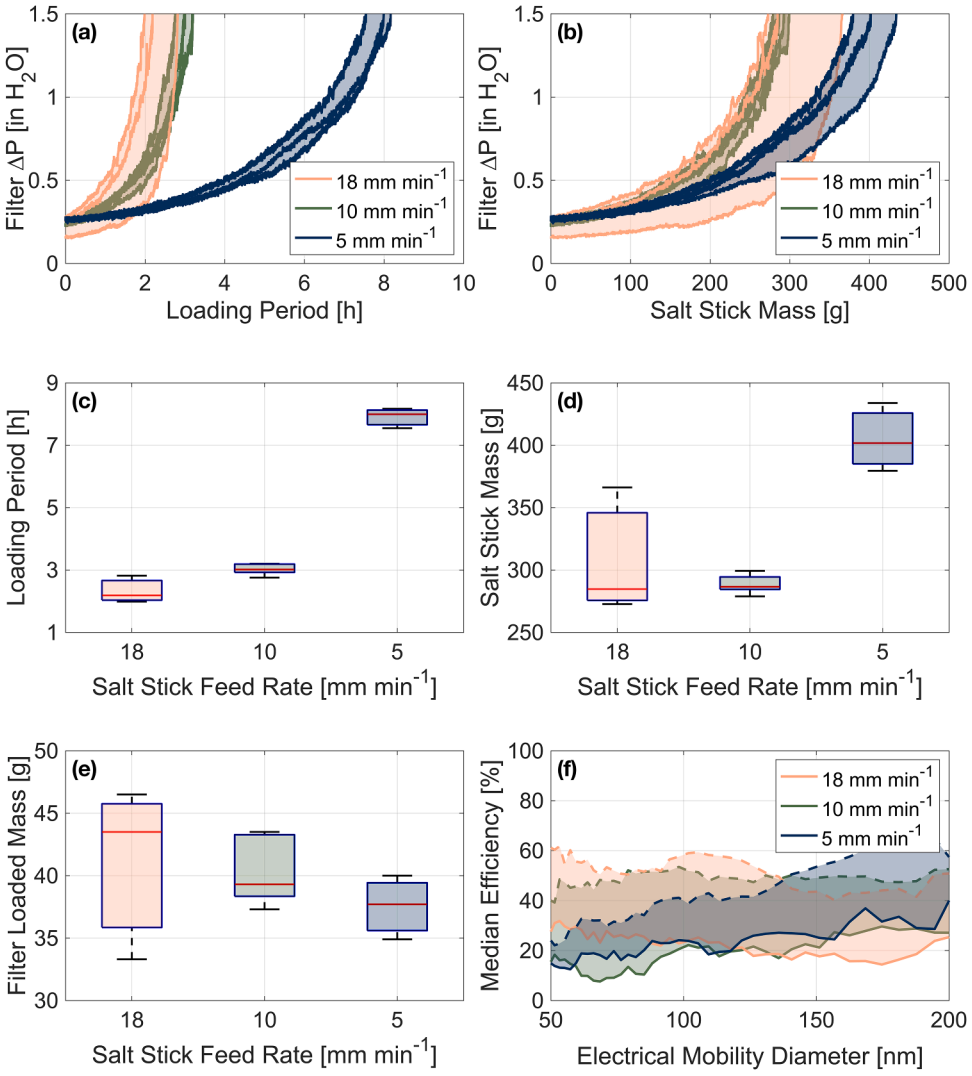

Fig. 10. Time-series plots (a, b), box plots (c to e), and filtration efficiency curves (f) of the submicron particle loading kinetics for MERV8 test-filters at different salt stick feed rate setpoints (pink color for 18 mm min^{-1}, green color for 10 mm min^{-1}, and blue color for 5 mm min^{-1}): (a) test-filter ΔP vs. loading period; (b) test-filter ΔP vs. the mass of salt sticks consumed by the TAG during the entire loading period; (c) summarized loading period for each salt stick feed rate setpoint; (d) summarized mass of salt sticks consumed for each salt stick feed rate setpoint; (e) change in the test-filter mass (loaded filter mass – initial filter mass) for each salt stick feed rate setpoint; (f) median initial filtration efficiency (solid line) and the final efficiency (dashed line). The time-series plots illustrate the real-time measurement of the test-filter ΔP at 1 Hz with three or five curves for each salt stick feed rate setpoint, each curve indicating an individual experiment at the salt stick feed rate loading condition and the shaded area showing the range that the replicate experiments enclosed. The box plots illustrate the median value (red line) and the interquartile range from the 25th to 75th percentile (blue box). The whiskers indicate the range of the remaining data, excluding outliers, which are plotted individually as red plus signs.

sensitivity of submicron-based loading to particle concentration and reinforces the suitability of KCl aerosol for realistic filter performance evaluations.

Fig. 9 illustrates the impact of salt stick feed rate on MERV13 filters. As with MERV14 filters, lower feed rates extended loading times while total salt stick consumption remained largely unchanged. At 18 mm min^{-1}, loading was completed in 0.8 ± 0.04 h, consuming 125.3 ± 2 g of salt stick mass, with a loaded mass of 76.8 ± 4 g. The baseline 10 mm min^{-1} feed rate resulted in a loading time of 1.3 ± 0.05 h, consuming 127.2 ± 6.4 g, with a loaded mass of 79.4 ± 2.7 g. At 5 mm min^{-1}, the loading time increased to 2.37 ± 0.07 h, with 119 ± 9.6 g of salt stick mass consumed and a loaded mass of 75.6 ± 2.7 g (Table 4). The similarity in DHC across feed rates indicates that particle feed rate has minimal impact on MERV13 performance, further validating the robustness of this method for long-term filter evaluation without bias from artificially high loading rates.

Fig. 10 shows the impact of feed rate on MERV8 filters. At 18 mm min^{-1}, loading was completed in 2.3 ± 0.43 h, consuming 307.9 ± 50.1 g of salt stick mass, with a loaded mass of 41.1 ± 7 g. The baseline 10 mm min^{-1} feed rate resulted in a 3.0 ± 0.18 h loading time, consuming 288.8 ± 7.7 g, with a loaded mass of 40.4 ± 2.8 g. At 5 mm min^{-1}, the loading time increased significantly to 7.9 ± 0.32 h, with 405 ± 27.3 g of salt stick mass consumed and a loaded mass of 37.5 ± 2.6 g (Table 4). As expected, lower feed rates extended loading time, but total salt stick consumption was similar at 18 mm min^{-1} and 10 mm min^{-1}. The difference at 5 mm min^{-1} likely stems from batch-to-batch variability in MERV8 filters.

The initial batch of MERV8 filters was used for five baseline tests and two tests at 18 mm min^{-1} before being exhausted. Later tests used a new batch provided by the manufacturer. While both batches were rated as MERV8, production differences and variations in efficiency assessments, especially given that the two batches were manufactured over five years apart, may explain discrepancies in filter loaded mass at 5 mm min^{-1}. It is possible that the second batch had slightly lower filtration efficiency

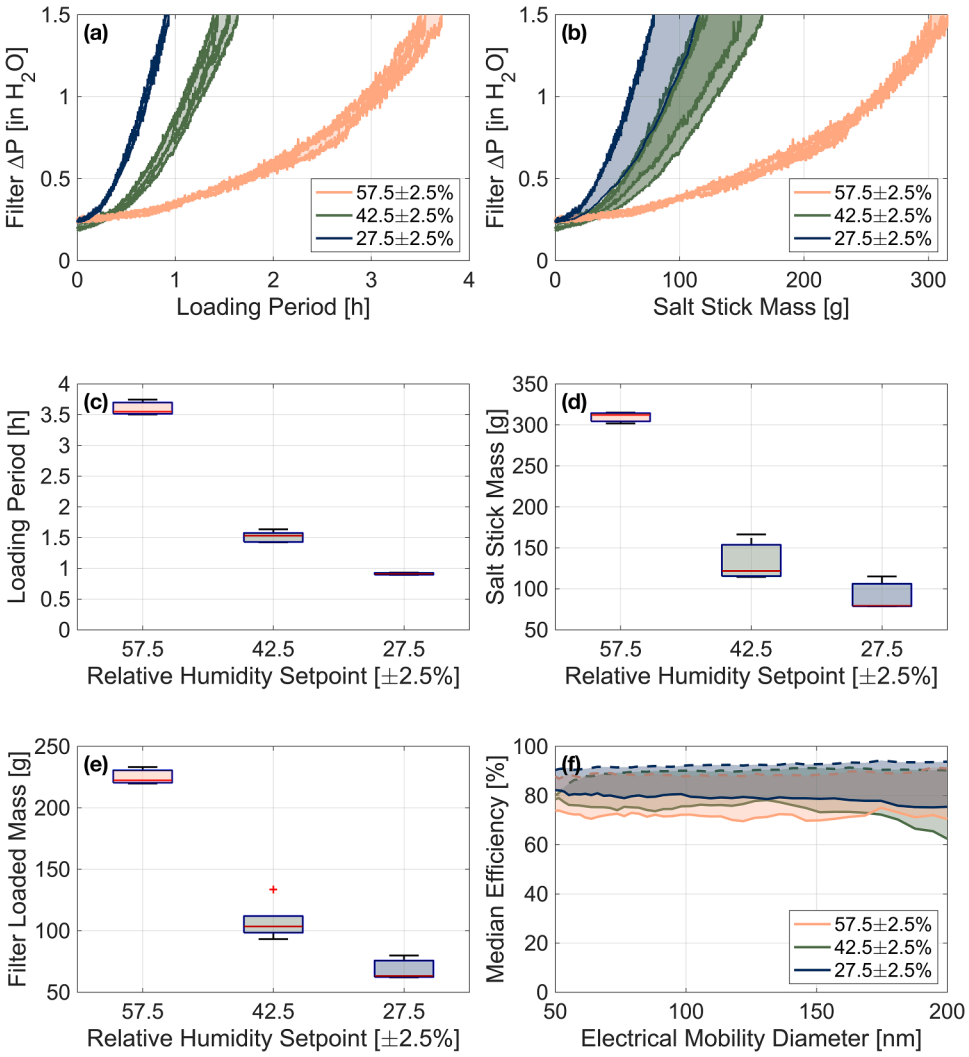

Fig. 11. Time-series plots (a, b), box plots (c to e), and filtration efficiency curves (f) of the submicron particle loading kinetics for MERV14 test-filters at different RH setpoints (pink color for 57.5 ± 2.5 % RH, green color for 42.5 ± 2.5 % RH, and blue color for 27.5 ± 2.5 % RH): (a) test-filter ΔP vs. loading period; (b) test-filter ΔP vs. the mass of salt sticks consumed by the TAG during the entire loading period; (c) summarized loading period for each RH setpoint; (d) summarized mass of salt sticks consumed for each RH setpoint; (e) change in the test-filter mass (loaded filter mass – initial filter mass) for each RH setpoint; (f) median initial filtration efficiency (solid line) and the final efficiency (dashed line). The time-series plots illustrate the real-time measurement of the test-filter ΔP at 1 Hz with three or five curves for each RH setpoint, each curve indicating an individual experiment at the RH loading condition and the shaded area showing the range that the replicate experiments enclosed. The box plots illustrate the median value (red line) and the interquartile range from the 25th to 75th percentile (blue box). The whiskers indicate the range of the remaining data, excluding outliers, which are plotted individually as red plus signs.

for submicron particles, leading to the observed differences.

3.4. Impact of relative humidity on filter loading performance

RH significantly influences filter loading behavior, with higher RH generally slowing the loading process [66–69,72,96–112]. This trend was observed across all test-filters in this study. Fig. 11 shows the impact of RH on MERV14 filter loading. At 57.5 ± 2.5 %, the loading time increased, requiring more salt stick consumption. This effect is likely due to changes in particle deposition and the morphology of dendrites on the filter media, which reduce airflow resistance and slow the increase in filter ΔP. While RH can alter particle size through hygroscopic growth [97,98,102,103,105,111], number-based PSDs remained generally consistent across all RH conditions in this study. The slight shift toward larger mass-based PSDs at lower RH is unlikely to be the primary driver of slower loading. Instead, enhanced particle-particle adhesive forces at higher RH appear to be the dominant factor [68].

Prior research supports this explanation. Joubert et al. (2010) [99] used scanning electron microscopy to show that NaCl particles adhere more closely under high RH, forming smaller dendritic structures that reduce filter ΔP growth. Li et al. (2020) [68] found that while RH minimally affects initial filtration efficiency, it slows filter ΔP evolution due to stronger adhesion between particles. At high RH, hygroscopic particles tend to stick to previously deposited particles rather than rolling into interstitial spaces, thereby slowing filter ΔP growth. Li et al. (2023) [109] further demonstrated that increased RH reduces dust cake drag coefficients via capillary coalescence, forming liquid bridges that create looser dust cakes with lower airflow resistance.

These effects primarily apply to hygroscopic particles like KCl and NaCl but not to non-hygroscopic aerosol. Boudhan et al. (2019) [104] observed greater ΔP growth for non-hygroscopic particles at higher RH, while Gupta et al. (1993) [105] and Montgomery et al. (2015) [66] reported minimal RH impact for aluminium oxide (Al_2O_3)-loaded filters. Gupta et al. (1993) [105] also noted that when RH exceeds the deliquescence point of hygroscopic particles, they transition into liquid form, filling filter media interstitial spaces and rapidly increasing ΔP. However, in this study, the RH remained well below deliquescence point for KCl, preventing liquid bridge formation. This aligns with Schwarz

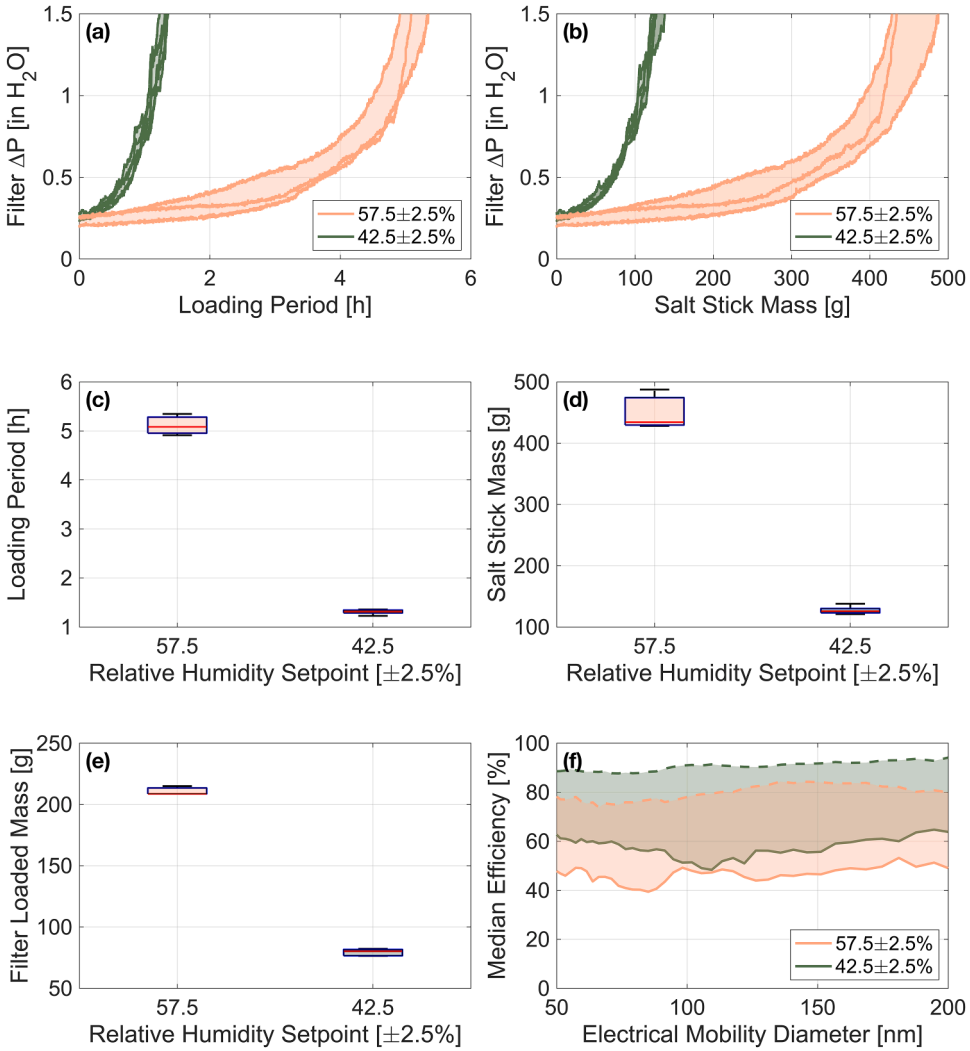

Fig. 12. Time-series plots (a, b), box plots (c to e), and filtration efficiency curves (f) of the submicron particle loading kinetics for MERV13 test-filters at different RH setpoints (pink color for 57.5 ± 2.5 % RH and green color for 42.5 ± 2.5 % RH): (a) test-filter ΔP vs. loading period; (b) test-filter ΔP vs. the mass of salt sticks consumed by the TAG during the entire loading period; (c) summarized loading period for each RH setpoint; (d) summarized mass of salt sticks consumed for each RH setpoint; (e) change in the test-filter mass (loaded filter mass – initial filter mass) for each RH setpoint; (f) median initial filtration efficiency (solid line) and the final efficiency (dashed line). The time-series plots illustrate the real-time measurement of the test-filter ΔP at 1 Hz with three or five curves for each RH setpoint, each curve indicating an individual experiment at the RH loading condition and the shaded area showing the range that the replicate experiments enclosed. The box plots illustrate the median value (red line) and the interquartile range from the 25th to 75th percentile (blue box). The whiskers indicate the range of the remaining data, excluding outliers, which are plotted individually as red plus signs.

et al. (2020) [106], who reported steep ΔP increases when filters were exposed to water droplets – an effect not observed under our conditions. In summary, the slower filter loading at higher RH is likely attributed to enhanced particle adhesion rather than significant changes in KCl aerosol size or morphology. These findings highlight the importance of RH in filter performance for hygroscopic aerosol under sub-deliquescent conditions.

Fig. 12 presents the impact of RH on MERV13 electret filter loading. As with MERV14 filters, higher RH resulted in longer loading times and greater salt stick consumption. However, the effect was more pronounced for MERV13 filters due to charge decay. High RH accelerates the loss of electrostatic charge in electret filter media, reducing their ability to capture particles via Coulombic and dielectrophoretic forces. This reduction in filtration efficiency suppresses the growth of filter ΔP. Liu et al. (2020) [112] observed a rapid decline in both surface potential and filtration efficiency after just one hour of exposure to 90 % RH, attributing this decline to charge dissipation. Similarly, Lee et al. (2020) [88] reported a loss of electrostatic charge within three minutes under similar conditions. In addition to charge decay, high RH increases dust cake porosity, further reducing ΔP growth. These combined effects explain why high RH has a stronger influence on MERV13 electret filters compared to mechanical filters like MERV14.

Fig. 13 shows that MERV8 filters also exhibited extended loading times at higher RH, consistent with trends observed for MERV14 and MERV13 filters. As a mechanical filter, MERV8 responded to high RH similarly to MERV14, with enhanced particle adhesion playing a dominant role in slowing the loading process. The strong RH dependence of KCl aerosol-based loading highlights a key distinction from traditional coarse dust loading methods, such as those specified in ANSI/ASHRAE Standard 52.2–2017 [70]. The broad RH range permitted by this standard (45 ± 10 %) resulted in significantly different loading behavior when applied to this submicron aerosol methodology. To minimize bias, this study implemented a stricter RH control range (±2.5 % per RH setpoint) ensuring greater consistency and reliability in evaluating filter performance under varying humidity conditions.

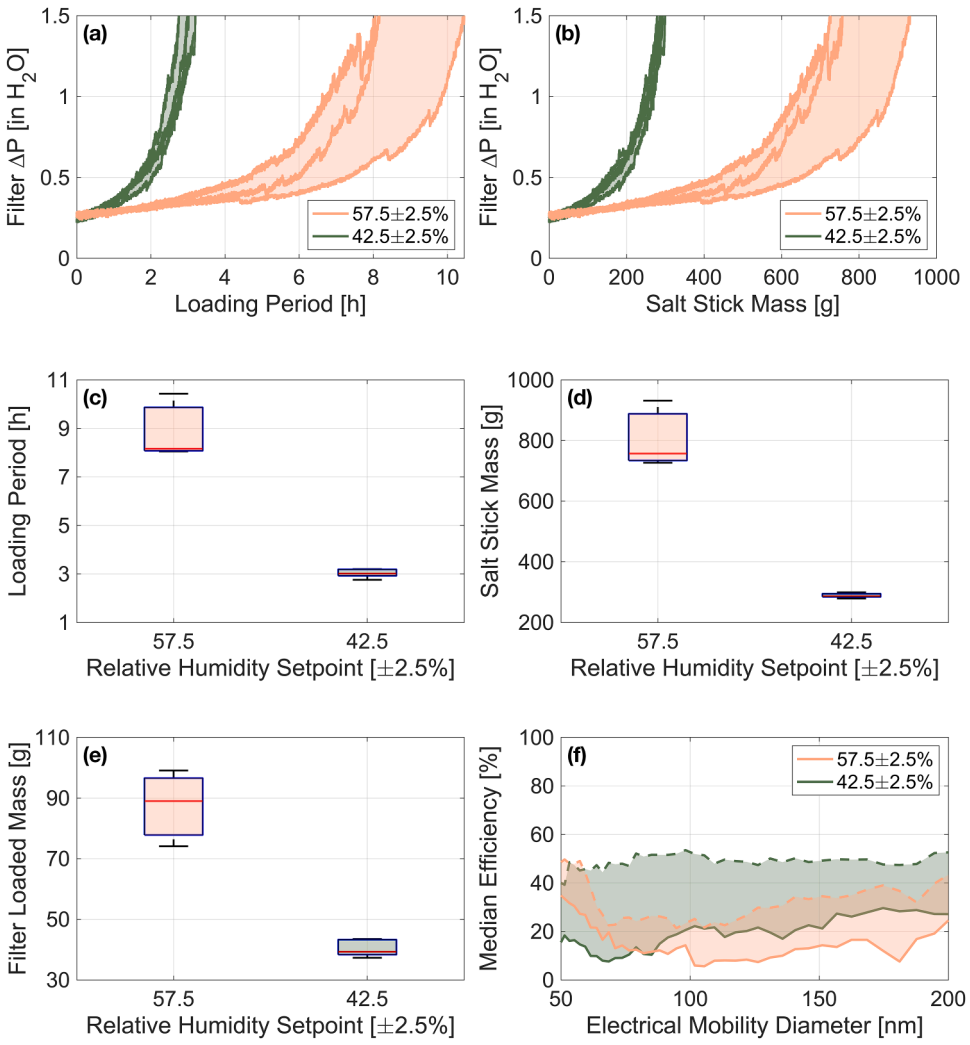

Fig. 13. Time-series plots (a, b), box plots (c to e), and filtration efficiency curves (f) of the submicron particle loading kinetics for MERV8 test-filters at different RH setpoints (pink color for 57.5 ± 2.5 % RH and green color for 42.5 ± 2.5 % RH): (a) test-filter ΔP vs. loading period; (b) test-filter ΔP vs. the mass of salt sticks consumed by the TAG during the entire loading period; (c) summarized loading period for each RH setpoint; (d) summarized mass of salt sticks consumed for each RH setpoint; (e) change in the test-filter mass (loaded filter mass – initial filter mass) for each RH setpoint; (f) median initial filtration efficiency (solid line) and the final efficiency (dashed line). The time-series plots illustrate the real-time measurement of the test-filter ΔP at 1 Hz with three or five curves for each RH setpoint, each curve indicating an individual experiment at the RH loading condition and the shaded area showing the range that the replicate experiments enclosed. The box plots illustrate the median value (red line) and the interquartile range from the 25th to 75th percentile (blue box). The whiskers indicate the range of the remaining data, excluding outliers, which are plotted individually as red plus signs.

4. Conclusions

This study evaluated the loading behavior of MERV8, MERV13, and MERV14 HVAC filters under various operational conditions – volumetric airflow rate, salt stick feed rate, and RH – using a new loading methodology with synthetic submicron KCl aerosol. The findings highlight how these factors influence filter ΔP evolution, loading time, and DHC, providing insights into filter performance and aging mechanisms. The airflow rate significantly affected filter loading. Higher airflow accelerated clogging and reduced loading time but consumed less salt stick mass due to finer KCl aerosol PSDs. Lower airflow prolonged loading and increased salt stick consumption due to slower clogging dynamics and larger particle sizes from extended in-duct residence times. This trend was consistent across filters, though MERV8 exhibited lower DHC due to its lower filtration efficiency. The salt stick feed rate had minimal impact on DHC across all filter types. While higher feed rates accelerated loading, total salt stick consumption and filter loaded mass remained comparable, demonstrating the robustness of the proposed TAG-based loading methodology in evaluating long-term performance without significant bias.

RH played a crucial role, particularly for hygroscopic KCl aerosol. Higher RH slowed loading across all filter types. For mechanical filters (MERV8, MERV14), increased particle adhesion led to looser dust cakes and suppressed ΔP growth. For electret filters (MERV13), high RH further reduced filtration efficiency by accelerating charge decay in addition to increasing dust cake porosity. These results underscore the importance of precise RH control in filter testing, with a stricter range (±2.5 %) ensuring consistency compared to the broader allowance of ANSI/ASHRAE Standard 52.2–2017.

This study successfully developed a repeatable filter loading methodology that better simulates real-world urban aerosol PSDs compared to conventional loading dusts. The findings improve understanding of filter aging and provide insights for optimizing HVAC system performance. Several aspects warrant further investigation. First, the electrostatic properties of TAG-generated KCl aerosol should be further examined, as particle charge can influence HVAC filter performance leading to bias in dust loading behavior, particularly for electret-based media like the MERV13 test-filters examined in this study.

Additionally, the presence of flame-generated ions may induce electrostatic charges on mechanical filters, potentially accelerating the improvement in filtration efficiency compared to scenarios involving neutral particles. Various aerosol measurement techniques have been used to measure particle charge properties [83,84,113,114]. Future work could explore charge-neutralization techniques, such as multiple neutralization sources [47], to enhance aerosol realism. Second, since absolute humidity (AH) may more directly affect filter performance than RH [104], its role in filter aging should be further studied. Moreover, the TAG output at a fixed setting produces only uni-modal PSDs, whereas urban aerosol typically exhibits broader, multi-modal PSDs. This discrepancy is anticipated to cause an underestimation in the filter ΔP growth rate and overestimation in the DHC, as detailed in a previous study [62]. Future research efforts could focus on incorporating multi-modal aerosol generation of variable organic and inorganic aerosol composites to further align laboratory-generated loading aerosol with real-world urban aerosol. Furthermore, instead of the bulk airflow rates in the test rig, future research is needed to examine the effects of face velocity and filtering velocity in greater detail. Lastly, improving RH stabilization (e.g., preheated humidifier water), optimizing the TAG salt stick feeding mechanism, and ensuring consistent filter selection within the same manufacturing lot would enhance experimental repeatability. Addressing these factors will further refine the proposed loading methodology and improve its applicability for HVAC filter evaluations.

CRediT authorship contribution statement

Chunxu Huang: Writing – review & editing, Writing – original draft, Visualization, Validation, Methodology, Investigation, Formal analysis, Data curation. **Nusrat Jung:** Writing – review & editing, Writing – original draft, Visualization, Validation, Supervision, Software, Resources, Project administration, Methodology, Investigation, Formal analysis, Data curation, Conceptualization. **Brandon E. Boor:** Writing – review & editing, Writing – original draft, Visualization, Supervision, Software, Resources, Methodology, Investigation, Formal analysis, Data curation, Conceptualization.

Declaration of competing interest

The authors declare that they have no conflict of interest.

Acknowledgments

This work was supported by the American Society of Heating, Refrigerating, and Air-Conditioning Engineers (ASHRAE) under Grant RP-1734. The authors are grateful for the support of the ASHRAE RP-1734 Project Monitoring Subcommittee: Paolo Tronville, Geoff Crosby, Bruce McDonald, Tom Justice, and Brian Krafthefer. The authors are grateful for the support of Ayesha Shah, David Rater, Hajin Park, Iane Loise Moreira Gomes, Laura Ajala, Brian H. Magnuson, Ekpeme Gbemiye-Etta, Caio K. Sugane Hamada, Susan L. Huster, Elliot P. Cram, and Ta-Kuan Chuang.

Data availability

Data will be made available on request.

References

[1] X. Ding, H. Lu, J. Jiang, A. Tasoglou, A.D. Shah, N. Jung, Real-time indoor sensing of volatile organic compounds during building disinfection events via photoionization detection and proton transfer reaction mass spectrometry, Build. Environ. 246 (2023) 110953, https://doi.org/10.1016/j.buildenv.2023.110953.

[2] J. Namiesnik, T. Goreckit, B. Kozdron-Zabiegala, J. Lukasiak, Indoor air quality (IAQ), pollutants, their sources and concentration levels, Build. Environ. 27 (3) (1992) 339–356, https://doi.org/10.1016/0360-1323(92)90034-M.

[3] S. Kamaruzzaman, N.A. Sabrani, The Effect of Indoor Air Quality (IAQ) Towards Occupants' Psychological Performance in Office Buildings, J. Rekabentuk Dan Binaan 4 (2011) 49–61.

[4] R.D. Brook, S. Rajagopalan, C.A. Pope, J.R. Brook, A. Bhatnagar, A.V. Diez-Roux, F. Holguin, Y. Hong, R.V. Luepker, M.A. Mittleman, A. Peters, D. Siscovick, S. C. Smith, L. Whitsel, J.D. Kaufman, Particulate matter air pollution and cardiovascular disease: an update to the scientific statement from the American Heart Association, Circulation 121 (2010) 2331–2378, https://doi.org/10.1161/CIR.0b013e3181dbece1.

[5] K.W. Tham, Indoor air quality and its effects on humans—a review of challenges and developments in the last 30 years, Energy Build. 130 (2016) 637–650, https://doi.org/10.1016/j.enbuild.2016.08.071.

[6] Z. Deng, B. Dong, X. Guo, J. Zhang, Impact of indoor air quality and multi-domain factors on human productivity and physiological responses: a comprehensive review, Indoor Air. (2024) 584960, https://doi.org/10.1155/2024/5584960.

[7] V. Van Tran, D. Park, Y.C. Lee, Indoor air pollution, related human diseases, and recent trends in the control and improvement of indoor air quality, Int. J. Env. Res. Public Health 17 (8) (2020) 2927, https://doi.org/10.3390/ijerph17082927.

[8] L. Tofful, S. Canepari, T. Sargolini, C. Perrino, Indoor air quality in a domestic environment: combined contribution of indoor and outdoor PM sources, Build. Environ. (2021) 108050, https://doi.org/10.1016/j.buildenv.2021.108050.

[9] W. Wang, R. Ooka, H. Kikumoto, W. Oh, M. Han, Influence of various factors on indoor/outdoor pollen concentration ratio based on experimental research: a review, Build. Environ. (2022) 109154, https://doi.org/10.1016/j.buildenv.2022.109154.

[10] D.A. Sterling, R.D. Lewis, Pollen and fungal spores indoor and outdoor of mobile homes, Ann. Allergy Asthma Immunol. 80 (1998) 279–285, https://doi.org/10.1016/S1081-1206(10)62971-7.

[11] I. Goh, J.P. Obbard, S. Viswanathan, Y. Huang, Airborne bacteria and fungal spores in the indoor environment. A case study in Singapore, Acta Biotechnol. 20 (2000) 67–73, https://doi.org/10.1002/abio.370200111.

[12] P.R. Tumminello, R. Niles, V. Valdez, C.K. Madawala, D.K. Gamage, K.A. Kimble, R.J. Leibensperger, C. Huang, C. Kaluarachchi, J. Dinasquet, F. Malfatti, C. Lee, G. B. Deane, M.D. Stokes, E. Stone, A. Tivanski, K.A. Prather, B.E. Boor, J.H. Slade, Size-dependent nascent sea spray aerosol bounce fractions and estimated viscosity: the role of divalent cation enrichment, surface tension, and the Kelvin effect, Environ. Sci. Technol. 58 (44) (2024) 19666–19678, https://doi.org/10.1021/acs.est.4c04312.

[13] K. O'Dell, B. Ford, J. Burkhardt, S. Magzamen, S.C. Anenberg, J. Bayham, E. V Fischer, J.R. Pierce, Outside in: the relationship between indoor and outdoor particulate air quality during wildfire smoke events in western US cities, Environ. Res.: Health 1 (2023) 015003, https://doi.org/10.1088/2752-5309/ac7d69.

[14] J. Jiang, N. Jung, B.E. Boor, Using building energy and smart thermostat data to evaluate indoor ultrafine particle source and loss processes in a net-zero energy house, ACS ES&T Eng. 1 (2021) 780–793, https://doi.org/10.1021/acsestengg.1c00002.

[15] S.S. Patra, J. Liu, J. Jiang, X. Ding, C. Huang, C. Keech, G. Steiner, P.S. Stevens, N. Jung, B.E. Boor, Rapid nucleation and growth of indoor atmospheric nanocluster aerosol during the use of scented volatile chemical products in residential buildings, ACS ES&T Air 1 (10) (2024) 1276–1293, https://doi.org/10.1021/acsestair.4c00118.

[16] S.S. Patra, J. Jiang, X. Ding, C. Huang, E.K. Reidy, V. Kumar, P. Price, C. Keech, G. Steiner, P. Stevens, N. Jung, B.E. Boor, Dynamics of nanocluster aerosol in the indoor atmosphere during gas cooking, PNAS Nexus 3 (2024) page044, https://doi.org/10.1093/pnasnexus/pgae044.

[17] J. Jiang, X. Ding, K.P. Isaacson, A. Tasoglou, H. Huber, A.D. Shah, N. Jung, B. E. Boor, Ethanol-based disinfectant sprays drive rapid changes in the chemical composition of indoor air in residential buildings, J. Hazard. Mater. Lett. 2 (2021) 100042, https://doi.org/10.1016/j.hazl.2021.100042.

[18] J. Jiang, X. Ding, S.S. Patra, J.N. Cross, C. Huang, V. Kumar, P. Price, E.K. Reidy, A. Tasoglou, H. Huber, P.S. Stevens, B.E. Boor, N. Jung, Siloxane emissions and exposures during the use of hair care products in buildings, Environ. Sci. Technol. 57 (2023) 19999–20009, https://doi.org/10.1021/acs.est.3c05156.

[19] J. Liu, J. Jiang, X. Ding, S.S. Patra, J.N. Cross, C. Huang, V. Kumar, P. Price, E. K. Reidy, A. Tasoglou, H. Huber, P.S. Stevens, B.E. Boor, N. Jung, Real-time evaluation of terpene emissions and exposures during the use of scented wax products in residential buildings with PTR-TOF-MS, Build. Environ. (2024) 111314, https://doi.org/10.1016/j.buildenv.2024.111314.

[20] C.F. Marciel Rosales, J. Jiang, A. Lahib, B.P. Bottorff, E.K. Reidy, V. Kumar, A. Tasoglou, H. Huber, S. Dusanter, A. Tomas, B.E. Boor, P.S. Stevens, Chemistry and human exposure implications of secondary organic aerosol production from indoor terpene ozonolysis, Sci. Adv. 8 (2022) eabj9156, https://doi.org/10.1126/sciadv.abj9156.

[21] S.S. Patra, T. Wu, D.N. Wagner, J. Jiang, B.E. Boor, Real-time measurements of fluorescent aerosol particles in a living laboratory office under variable human occupancy and ventilation conditions, Build. Environ. (2021) 108249, https://doi.org/10.1016/j.buildenv.2021.108249.

[22] P. Azimi, B. Stephens, HVAC filtration for controlling infectious airborne disease transmission in indoor environments: predicting risk reductions and operational costs, Build. Environ. 70 (2013) 150–160, https://doi.org/10.1016/j.buildenv.2013.08.025.

[23] P. Zhao, J.A. Siegel, R.L. Corsi, Ozone removal by HVAC filters, Atmos Environ. 41 (2007) 3151–3160, https://doi.org/10.1016/j.atmosenv.2006.06.059.

[24] T. Wu, A. Tasoglou, D.N. Wagner, J. Jiang, H.J. Huber, P.S. Stevens, N. Jung, B. E. Boor, Modern buildings act as a dynamic source and sink for urban air

pollutants, Cell Rep. Sustain. 1 (2024) 100103, https://doi.org/10.1016/j.crsus.2024.100103.
[25] M. Zaatari, A. Novoselac, J. Siegel, The relationship between filter pressure drop, indoor air quality, and energy consumption in rooftop HVAC units, Build. Environ. 73 (2014) 151–161, https://doi.org/10.1016/j.buildenv.2013.12.010.
[26] J.F. Montgomery, S.I. Green, S.N. Rogak, K. Bartlett, Predicting the energy use and operation cost of HVAC air filters, Energy Build. 47 (2012) 643–650, https://doi.org/10.1016/j.enbuild.2012.01.001.
[27] W.J. Fisk, D. Faulkner, J. Palonen, O. Seppanen, Performance and costs of particle air filtration technologies, Indoor Air. 12 (2002) 223–234, https://doi.org/10.1034/j.1600-0668.2002.01136.x.
[28] S. Pöyhönen, J. Ahola, M. Niemelä, S. Hammo, P. Punnonen, Variable-speed-drive-based method for the cost optimization of air filter replacement timing, Energy Build. (2021) 110904, https://doi.org/10.1016/j.enbuild.2021.110904.
[29] Z. Feng, Z. Long, Q. Chen, Assessment of various CFD models for predicting airflow and pressure drop through pleated filter system, Build. Environ. 75 (2014) 132–141, https://doi.org/10.1016/j.buildenv.2014.01.022.
[30] F.I. Abam, S.O. Effiom, O.S. Ohunakin, CFD evaluation of pressure drop across a 3-D filter housing for industrial gas turbine plants, Front. Energy 10 (2016) 192–202, https://doi.org/10.1007/s11708-016-0406-x.
[31] B. Stephens, A. Novoselac, J.A. Siegel, The effects of filtration on pressure drop and energy consumption in residential HVAC systems (RP-1299), HVAC&R Res. 16 (2010) 273–294, https://doi.org/10.1080/10789669.
[32] M. Alavy, J.A. Siegel, IAQ and energy implications of high efficiency filters in residential buildings: a review (RP-1649), Sci. Technol. Built. Environ. 25 (2019) 261–271, https://doi.org/10.1080/23744731.2018.1526012.
[33] M. Alavy, T. Li, J.A. Siegel, Energy use in residential buildings: analyses of high-efficiency filters and HVAC fans, Energy Build. 209 (2020) 109697, https://doi.org/10.1016/j.enbuild.2019.109697.
[34] N. Nassif, The impact of air filter pressure drop on the performance of typical air-conditioning systems, Build. Simul. 5 (2012) 345–350, https://doi.org/10.1007/s12273-012-0091-6.
[35] T. Li, J.A. Siegel, The impact of control strategies on filtration performance, Energy Build. 252 (2021) 111378, https://doi.org/10.1016/j.enbuild.2021.111378.
[36] W.W.F. Leung, C.H. Hung, Investigation on pressure drop evolution of fibrous filter operating in aerodynamic slip regime under continuous loading of sub-micron aerosols, Sep. Purif. Technol. 63 (2008) 691–700, https://doi.org/10.1016/j.seppur.2008.07.015.
[37] S. Fotovati, S.A. Hosseini, H. Vahedi Tafreshi, B. Pourdeyhimi, Modeling instantaneous pressure drop of pleated thin filter media during dust loading, Chem. Eng. Sci. 66 (2011) 4036–4046, https://doi.org/10.1016/j.ces.2011.05.038.
[38] D.R. Chen, D.Y.H. Pui, B.Y.H. Liu, Optimization of pleated filter designs using a finite-element numerical model, Aerosol. Sci. Technol. 23 (1995) 579–590, https://doi.org/10.1080/02786829508965339.
[39] M. Rebai, M. Prat, M. Meireles, P. Schmitz, R. Baclet, Clogging modeling in pleated filters for gas filtration, Chem. Eng. Res. Des. 88 (2010) 476–486, https://doi.org/10.1016/j.cherd.2009.08.014.
[40] F. Qian, N. Huang, J. Lu, Y. Han, CFD-DEM simulation of the filtration performance for fibrous media based on the mimic structure, Comput. Chem. Eng. 71 (2014) 478–488, https://doi.org/10.1016/j.compchemeng.2014.09.018.
[41] Y. Zhang, T. Li, J.A. Siegel, Investigating the impact of filters on long-term particle concentration measurements in residences (RP-1649), Sci. Technol. Built. Environ. 26 (2020) 1037–1047, https://doi.org/10.1080/23744731.2020.1778402.
[42] T. Li, J. Siegel, Laboratory performance of new and used residential HVAC filters: comparison to field results (RP-1649), Sci. Technol. Built. Environ. 26 (2020) 844–855, https://doi.org/10.1080/23744731.2020.1738871.
[43] T. Wu, B.E. Boor, Urban aerosol size distributions: a global perspective, Atmos. Chem. Phys. 21 (2021) 8883–8914, https://doi.org/10.5194/acp-21-8883-2021.
[44] W. Poon, B. Liu, Dust loading behavior of engine and general purpose air cleaning filters, SAE Tech. Paper (1997) 970676, https://doi.org/10.4271/970674.
[45] W. Poon, B. Liu, A bimodal loading test for engine and general purpose air cleaning filters, SAE Tech. Paper. (1997) 970674, https://doi.org/10.4271/970674.
[46] J.K. Lee, S.C. Kim, B.Y.H. Liu, Effect of bi-modal aerosol mass loading on the pressure drop for gas cleaning industrial filters, Aerosol Sci. Technol. 35 (2001) 805–814, https://doi.org/10.1080/027868201753227352.
[47] P.K. Giffin, M.S. Parsons, R.J. Unz, C.A. Waggoner, Large-scale generic test stand for testing of multiple configurations of air filters utilizing a range of particle size distributions, Rev. Sci. Instrum. 83 (5) (2012) 055105, https://doi.org/10.1063/1.4717671.
[48] Q. Wang, X. Lin, D.R. Chen, Effect of dust loading rate on the loading characteristics of high efficiency filter media, Powder. Technol. 287 (2016) 20–28, https://doi.org/10.1016/j.powtec.2015.09.032.
[49] T. Valmari, M. Lehtimäki, A. Taipale, Filter clogging by bimodal aerosol, Aerosol Sci. Technol. 40 (2006) 255–260, https://doi.org/10.1080/02786820500543282.
[50] Y. Endo, D.-R. Chen, D.Y.H. Pui, Effects of particle polydispersity and shape factor during dust cake loading on air filters, Powder. Technol. 98 (1998) 241–249, https://doi.org/10.1016/S0032-5910(98)00063-1.
[51] Y. Endo, D.-R. Chen, D.Y.H. Pui, Bimodal aerosol loading and dust cake formation on air filters, Filtr. Sep. 35 (1998) 191–195, https://doi.org/10.1016/S0015-1882(98)91369-6.
[52] S.C. Kim, J. Wang, W.G. Shin, J.H. Scheckman, D.Y.H. Pui, Structural properties and filter loading characteristics of soot agglomerates, Aerosol. Sci. Technol. 43 (2009) 1033–1041, https://doi.org/10.1080/02786820903131081.
[53] X. Tian, Q. Ou, J. Liu, Y. Liang, D.Y.H. Pui, Particle loading characteristics of a two-stage filtration system, Sep. Purif. Technol. 215 (2019) 351–359, https://doi.org/10.1016/j.seppur.2019.01.033.
[54] G. Berry, I. Beckman, H. Cho, A comprehensive review of particle loading models of fibrous air filters, J. Aerosol. Sci. 167 (6) (2023) 106078, https://doi.org/10.1016/j.jaerosci.2022.106078.
[55] A.Y. Al-Otoom, Prediction of the collection efficiency, the porosity, and the pressure drop across filter cakes in particulate air filtration, Atmos. Environ. 39 (2005) 51–57, https://doi.org/10.1016/j.atmosenv.2004.09.057.
[56] D. Thomas, P. Penicot, P. Contal, D. Leclerc, J. Vendel, Clogging of fibrous filters by solid aerosol particles experimental and modelling study, Chem. Eng. Sci. 56 (2001) 3549–3561, https://doi.org/10.1016/S0009-2509(01)00041-0.
[57] R. Arunkumar, K.U. Hogancamp, M.S. Parsons, D.M. Rogers, O.P. Norton, B. A. Nagel, S.L. Alderman, C.A. Waggoner, High-efficiency particulate air filter test stand and aerosol generator for particle loading studies, Rev. Sci. Instrum. 78 (8) (2007) 085105, https://doi.org/10.1063/1.2771421.
[58] P. Bulejko, O. Krištof, M. Dohnal, An assessment on average pressure drop and dust-holding capacity of hollow-fiber membranes in air filtration, Membranes 11 (7) (2021) 467, https://doi.org/10.3390/membranes11070467.
[59] Q. Li, Z. Wang, S. Shao, Z. Niu, Y. Xin, D. Zhao, Y. Hou, Z. Xu, Experimental study on the synthetic dust loading characteristics of air filters, Sep. Purif. Technol. 284 (2022) 120209, https://doi.org/10.1016/j.seppur.2021.120209.
[60] T. Wu, B.E. Boor, Characterization of a thermal aerosol generator for HVAC filtration experiments (RP-1734), Sci. Technol. Built. Environ. 26 (2020) 816–834, https://doi.org/10.1080/23744731.2020.1730661.
[61] Z. Zhang, F. Jiang, In-place HEPA filter testing by the sodium flame method, Powder. Technol. 301 (2016) 615–621, https://doi.org/10.1016/j.powtec.2016.06.046.
[62] C. Huang, B.E. Boor, Integration of a thermal aerosol generator into a full-scale HVAC filter test rig for aging filters with representative urban aerosol size distributions (RP-1734), Sci. Technol. Built. Environ. (2025).
[63] T. Xia, Y. Bian, L. Zhang, C. Chen, Relationship between pressure drop and face velocity for electrospun nanofiber filters, Energy Build. 158 (2018) 987–999, https://doi.org/10.1016/j.enbuild.2017.10.073.
[64] Y. Bian, L. Zhang, C. Chen, Experimental and modeling study of pressure drop across electrospun nanofiber air filters, Build. Environ. 142 (2018) 244–251, https://doi.org/10.1016/j.buildenv.2018.06.021.
[65] P. Abdolghader, C. Brochot, F. Haghighat, A. Bahloul, Airborne nanoparticles filtration performance of fibrous media: a review, Sci. Technol. Built. Environ. 24 (2018) 648–672, https://doi.org/10.1080/23744731.2018.1452454.
[66] J.F. Montgomery, S.I. Green, S.N. Rogak, Impact of relative humidity on HVAC filters loaded with hygroscopic and non-hygroscopic particles, Aerosol. Sci. Technol. 49 (2015) 322–331, https://doi.org/10.1080/02786826.2015.1026433.
[67] X. He, B.T. Brem, Y.K. Bahk, Y.Y. Kuo, J. Wang, Effects of relative humidity and particle type on the performance and service life of automobile cabin air filters, Aerosol. Sci. Technol. 50 (2016) 542–554, https://doi.org/10.1080/02786826.2016.1167832.
[68] S. Li, D.R. Chen, F. Zhou, S.C. Chen, Effects of relative humidity and particle hygroscopicity on the initial efficiency and aging characteristics of electret HVAC filter media, Build. Environ. 171 (2020) 106669, https://doi.org/10.1016/j.buildenv.2020.106669.
[69] C. Pei, Q. Ou, D.Y.H. Pui, Effects of temperature and relative humidity on laboratory air filter loading test by hygroscopic salts, Sep. Purif. Technol. 255 (2021) 117679, https://doi.org/10.1016/J.SEPPUR.2020.117679.
[70] ASHRAE, Method of Testing General Ventilation Air-Cleaning Devices for Removal Efficiency by Particle Size, in: ANSI/ASHRAE 52.2-2017, Atlanta, GA, 2017.
[71] D. Thomas, R.P. Contal, V. Renaudin, P. Penicot, D. Leclerc, J. Vendels, Modelling pressure drop in hepa filters during dynamic filtration, J. Aerosol. Sci. 30 (1999) 235–246, https://doi.org/10.1016/S0021-8502(98)00036-6.
[72] B. Xu, Y. Wu, Z. Lin, Z. Chen, Investigation of air humidity affecting filtration efficiency and pressure drop of vehicle cabin air filters, Aerosol. Air. Qual. Res. 14 (2014) 1066–1073, https://doi.org/10.4209/aaqr.2013.06.0204.
[73] ASHRAE, Standard Methods for Air Velocity and Airflow Measurement, in: ANSI/ASHRAE Standard 41.2-2022, Atlanta, GA, 2022.
[74] B. Stephens, J.A. Siegel, Ultrafine particle removal by residential heating, ventilating, and air-conditioning filters, Indoor Air. 23 (2013) 488–497, https://doi.org/10.1111/ina.12045.
[75] T. Fazli, Y. Zeng, B. Stephens, Fine and ultrafine particle removal efficiency of new residential HVAC filters, Indoor Air. 29 (2019) 656–669, https://doi.org/10.1111/ina.12566.
[76] W.C. Hinds, Y. Zhu, Aerosol Technology: Properties, Behavior, and Measurement of Airborne Particles, 3rd ed., John Wiley & Sons, 2022.
[77] J.H. Ji, G.N. Bae, S.H. Kang, J. Hwang, Effect of particle loading on the collection performance of an electret cabin air filter for submicron aerosols, J. Aerosol. Sci. 34 (2003) 1493–1504, https://doi.org/10.1016/S0021-8502(03)00103-4.
[78] F.J. Romay, B.Y.H. Liu, S.J. Chae, Experimental study of electrostatic capture mechanisms in commercial electret filters, Aerosol. Sci. Technol. 28 (1998) 224–234, https://doi.org/10.1080/02786829808965523.
[79] N.R. Mukherjee, T. Fueno, H. Eyring, T. Ree, Ions in flames, Symp. (Int.) Combust. 8 (1961) 1–22, https://doi.org/10.1016/S0082-0784(06)80482-0.

[80] A.B. Fialkov, Y. Str, K. Kazakstan, Investigations on ions in Flames, Prog. Energy Combust. Sci. 23 (1997) 399–528, https://doi.org/10.1016/S0360-1285(97)00016-6.
[81] H.R. Paur, W. Baumann, H. Mätzing, H. Seifert, Formation of nanoparticles in flames; measurement by particle mass spectrometry and numerical simulation, Nanotechnol. 16 (7) (2005) S354–61, https://doi.org/10.1088/0957-4484/16/7/007.
[82] N.A. Fuchs, On the stationary charge distribution on aerosol particles in a bipolar ionic atmosphere, Geofis. Pura Appl. 56 (1963) 185–193, https://doi.org/10.1007/BF01993343.
[83] Y. Wang, G. Sharma, C. Koh, V. Kumar, R. Chakrabarty, P. Biswas, Influence of flame-generated ions on the simultaneous charging and coagulation of nanoparticles during combustion, Aerosol. Sci. Technol. 51 (2017) 833–844, https://doi.org/10.1080/02786826.2017.1304635.
[84] C. Bagya Ramesh, Y. Wang, Ions generated from a premixed methane-air flame: mobility size distributions and charging characteristics, Combust. Sci. Technol. 196 (16) (2023) 4041–4056, https://doi.org/10.1080/00102202.2023.2203818.
[85] R. Thakur, D. Das, A. Das, Electret air filters, Sep. Purif. Rev. 42 (2013) 87–129, https://doi.org/10.1080/15422119.2012.681094.
[86] J. Pich, H. Emi, C. Kanaoka, Coulombic deposition mechanism in electret filters, J. Aerosol Sci. 18 (1) (1987) 29–35, https://doi.org/10.1016/0021-8502(87)90006-1.
[87] A. Kilic, S. Russell, E. Shim, B. Pourdeyhimi, The charging and stability of electret filters. Fibrous Filter Media, Elsevier Inc., 2017, pp. 95–121, https://doi.org/10.1016/B978-0-08-100573-6.00025-3.
[88] J. Lee, J. Kim, Material properties influencing the charge decay of electret filters and their impact on filtration performance, Polymers 12 (2020) 721, https://doi.org/10.3390/polym12030721.
[89] M. Liu, D.E. Claridge, S. Deng, An air filter pressure loss model for fan energy calculation in air handling units, Int. J. Energy Res. 27 (2003) 589–600, https://doi.org/10.1002/er.897.
[90] M. Lupion, B. Alonso-Fariñas, M. Rodriguez-Galan, B. Navarrete, Modelling pressure drop evolution on high temperature filters, Chem. Eng. Process.: Process. Intensif. 66 (2013) 12–19, https://doi.org/10.1016/j.cep.2013.01.010.
[91] P.J. García Nieto, E. García-Gonzalo, G. Arbat, M. Duran-Ros, F. Ramírez de Cartagena, J. Puig-Bargués, Pressure drop modelling in sand filters in micro-irrigation using gradient boosted regression trees, Biosyst. Eng. 171 (2018) 41–51, https://doi.org/10.1016/j.biosystemseng.2018.04.011.
[92] R.D. Rivers, D.J. Murphy Jr. Air filter performance under variable air volume conditions, ASHRAE Trans. 106 (2000) 131, https://www.proquest.com/scholarly-journals/air-filterperformance-under-variable-volume/docview/192519486/se-2.
[93] O.F. Eker, F. Camci, I.K. Jennions, Physics-based degradation modelling for filter clogging, in: PHM Society European Conference, 2014, https://doi.org/10.36001/phme.2014.v2i1.1478.
[94] H. Alimohammadi, K. Vassiljeva, E. Petlenkov, M. Thalfeldt, A. Mikola, T.M. Kull, A. Köse, Gray box time variant clogging behaviour and pressure drop prediction of the air filter in the HVAC system, in: E3S Web of Conferences, EDP Sci. (2021), https://doi.org/10.1051/e3sconf/202124610002.
[95] H. Zhang, J. Liu, X. Zhang, C. Huang, X. Jin, Design of electret polypropylene melt blown air filtration material containing nucleating agent for effective PM2.5 capture, RSC. Adv. 8 (2018) 7932–7941, https://doi.org/10.1039/c7ra10916d.
[96] D.C. Walsh, J.I.T. Stenhouse, The effect of particle size, charge, and composition on the loading characteristics of an electrically active fibrous filter material, J. Aerosol. Sci. 28 (1997) 307–321, https://doi.org/10.1016/S0021-8502(96)00434-X.
[97] B.E. Cummings, Y. Li, P.F. Decarlo, M. Shiraiwa, M.S. Waring, Indoor aerosol water content and phase state in U.S. residences: impacts of relative humidity, aerosol mass and composition, and mechanical system operation, Env. Sci. Process. Impacts 22 (2020) 2031–2057, https://doi.org/10.1039/d0em00122h.
[98] E. Weingartner, U. Baltensperger, H. Burtscher, Growth and structural change of combustion aerosols at high relative humidity, Environ. Sci. Technol. 29 (1995) 2982–2986, https://doi.org/10.1021/es00012a014.
[99] A. Joubert, J.C. Laborde, L. Bouilloux, S. Callé-Chazelet, D. Thomas, Influence of humidity on clogging of flat and pleated HEPA filters, Aerosol. Sci. Technol. 44 (2010) 1065–1076, https://doi.org/10.1080/02786826.2010.510154.
[100] J.F. Montgomery, S.N. Rogak, S.I. Green, Y. You, A.K. Bertram, Structural change of aerosol particle aggregates with exposure to elevated relative humidity, Environ. Sci. Technol. 49 (2015) 12054–12061, https://doi.org/10.1021/acs.est.5b03157.
[101] D. Hu, L. Qiao, J. Chen, X. Ye, X. Yang, T. Cheng, W. Fang, Hygroscopicity of inorganic aerosols: size and relative humidity effects on the growth factor, Aerosol. Air. Qual. Res. 10 (2010) 255–264, https://doi.org/10.4209/aaqr.2009.12.0076.
[102] P.H. McMurry, M.R. Stolzenburg, On the sensitivity of particle size to relative humidity for Los Angeles aerosols, Atmos. Environ. 23 (1989) (1967) 497–507, https://doi.org/10.1016/0004-6981(89)90593-3.
[103] T. Reponen, K. Willeke, V. Ulevicius, A. Reponen, S.A. Grinshpun, Effect of relative humidity on the aerodynamic diameter and respiratory deposition of fungal spores, Atmos. Environ. 30 (1996) 3967–3974, https://doi.org/10.1016/1352-2310(96)00128-8.
[104] R. Boudhan, A. Joubert, S. Durécu, K. Gueraoui, L.Le Coq, Influence of air humidity on particle filtration performance of a pulse-jet bag filter, J. Aerosol. Sci. 130 (2019) 1–9, https://doi.org/10.1016/j.jaerosci.2019.01.002.
[105] A. Gupta, V.J. Novick, P. Biswas, P.R. Monson, Effect of humidity and particle hygroscopicity on the mass loading capacity of high efficiency particulate air (HEPA) filters, Aerosol. Sci. Technol. 19 (1993) 94–107, https://doi.org/10.1080/02786829308959624.
[106] A.D. Schwarz, L. König, J. Meyer, A. Dittler, Impact of water droplet and humidity interaction with soluble particles on the operational performance of surface filters in gas cleaning applications, J. Aerosol. Sci. 142 (2020) 105523, https://doi.org/10.1016/j.jaerosci.2020.105523.
[107] A.F. Miguel, Effect of air humidity on the evolution of permeability and performance of a fibrous filter during loading with hygroscopic and non-hygroscopic particles, J. Aerosol. Sci. 34 (2003) 783–799, https://doi.org/10.1016/S0021-8502(03)00027-2.
[108] J. Li, F. Zhou, S. Li, Experimental study on the dust filtration performance with participation of water mist, Process Saf. Environ. Prot. 109 (2017) 357–364, https://doi.org/10.1016/j.psep.2017.04.006.
[109] S. Li, Y. Lin, M. Han, H. Liu, J. Shao, X. Tan, Y. Luo, R. Huang, Effects of various wet environments on the characteristics of the dust cake deposited on the surface of filter media, Sci. Rep. 13 (1) (2023) 17120, https://doi.org/10.1038/s41598-023-44429-4.
[110] D. Shi, J. Li, Y. Du, Q. Wu, S. Huang, H. Huang, D. Wu, Influence of relative humidity on the characteristics of filter cake using particle flow code simulation, Atmosphere 13 (5) (2022) 770, https://doi.org/10.3390/atmos13050770.
[111] J.F. Peng, M. Hu, Z.B. Wang, X.F. Huang, P. Kumar, Z.J. Wu, S. Guo, D.L. Yue, D. J. Shang, Z. Zheng, L.Y. He, Submicron aerosols at thirteen diversified sites in China: size distribution, new particle formation and corresponding contribution to cloud condensation nuclei production, Atmos. Chem. Phys. 14 (2014) 10249–10265, https://doi.org/10.5194/acp-14-10249-2014.
[112] C. Liu, Z. Dai, B. He, Q.F. Ke, The effect of temperature and humidity on the filtration performance of electret melt-blown nonwovens, Materials 13 (2020) 4774, https://doi.org/10.3390/ma13214774.
[113] W. Glover, H.K. Chan, Electrostatic charge characterization of pharmaceutical aerosols using electrical low-pressure impaction (ELPI), J. Aerosol. Sci. 35 (2004) 755–764, https://doi.org/10.1016/j.jaerosci.2003.12.003.
[114] L.A. Sgro, A. D'Anna, P. Minutolo, Charge distribution of incipient flame-generated particles, Aerosol Sci. Technol. 44 (2010) 651–662, https://doi.org/10.1080/02786826.2010.483701.